remote sensing

MDPI

Article

First Measurements of Gas Flux with a Low-Cost Smartphone Sensor-Based UV Camera on the Volcanoes of Northern Chile

Felipe Aguilera [1,2,3,*], Susana Layana [1,3,4], Felipe Rojas [1], Pilar Arratia [1], Thomas C. Wilkes [5], Cristóbal González [1,4], Manuel Inostroza [1,4], Andrew J.S. McGonigle [5], Tom D. Pering [5] and Gabriel Ureta [1,3,4]

1 Núcleo de Investigación en Riesgo Volcánico—Ckelar Volcanes, Universidad Católica del Norte, Avenida Angamos 0610, Antofagasta 1270709, Chile; susana.layana@alumnos.ucn.cl (S.L.); frv013@alumnos.ucn.cl (F.R.); pah016@alumnos.ucn.cl (P.A.); cristobal.gonzalez@alumnos.ucn.cl (C.G.); manuel.inostroza@alumnos.ucn.cl (M.I.); gabriel.ureta@ucn.cl (G.U.)
2 Departamento de Ciencias Geológicas, Universidad Católica del Norte, Avenida Angamos 0610, Antofagasta 1270709, Chile
3 Centro de Investigación para la Gestión Integrada del Riesgo de Desastres (CIGIDEN), Av. Vicuña Mackenna 4860, Santiago 7810000, Chile
4 Programa de Doctorado en Ciencias mención Geología, Universidad Católica del Norte, Avenida Angamos 0610, Antofagasta 1270709, Chile
5 Department of Geography, The University of Sheffield, Western Bank, Sheffield S10 2TN, UK; tcwilkes1@sheffield.ac.uk (T.C.W.); a.mcgonigle@sheffield.ac.uk (A.J.S.M.); t.pering@sheffield.ac.uk (T.D.P.)
* Correspondence: feaguilera@ucn.cl

Received: 25 April 2020; Accepted: 29 June 2020; Published: 2 July 2020

Abstract: UV cameras have been used for over a decade in order to remotely sense SO_2 emission rates from active volcanoes, and to thereby enhance our understanding of processes related to active and passive degassing. Whilst SO_2 column density retrievals can be more accurate/sophisticated using alternative techniques (e.g., Differential Optical Absorption Spectrometer (DOAS), Correlation Spectrometer (COSPEC)), due to their higher spectral resolutions, UV cameras provide the advantage of high time-resolution emission rates, a much greater spatial resolution, and the ability to simultaneously retrieve plume speeds. Nevertheless, the relatively high costs have limited their uptake to a limited number of research groups and volcanic observatories across the planet. One recent intervention in this regard has been the introduction of the PiCam UV camera, which has considerably lowered instrumental cost. Here we present the first data obtained with the PiCam system from seven persistently degassing volcanoes in northern Chile, demonstrating robust field operation in challenging conditions and over an extended period of time, hence adding credence to the potential of these units for more widespread dissemination to the international volcanic gas measurement community. Small and weak plumes, as well as strongly degassing plumes were measured at distances ranging 0.6–10.8 km from the sources, resulting in a wide range of SO_2 emission rates, varying from 3.8 ± 1.8 to 361 ± 31.6 td^{-1}. Our acquired data are discussed with reference to previously reported emission rates from other ground-based remotely sensed techniques at the same volcanoes, in particular considering: resolution of single plume emissions in multi-plume volcanoes, light dilution, plume geometry, seasonal effects, and the applied plume speed measurement methodology. The main internal/external factors that influence positive/negative PiCam measurements include camera shake, light dilution, and the performance of the OpenCV and control points post processing methods. A simple reprocessing method is presented in order to correct the camera shake. Finally, volcanoes were separated into two distinct groups: low and moderate SO_2 emission rates systems. These groups correlate positively with their volcanological characteristics, especially with the fluid compositions from fumaroles.

Keywords: PiCam; central volcanic zone; SO_2 emission rates; volcanic degassing; Andes

1. Introduction

Sulfur dioxide (SO_2) is a toxic gas arising from various anthropogenic sources, which is also emitted from persistently degassing and eruptive volcanoes, leading to significant potential impacts upon the environment and local economies [1]. SO_2 from volcanoes is typically the third most abundant volatile in released gas plumes, after H_2O and CO_2 (e.g., [2]), typically accounting for some 2–12% of the molar mass (e.g., [3]). SO_2 emission rates and their fluctuations can indicate possible changes in underground magma flux [4], and are considered as proxies for eruptions [5]. SO_2 has been measured and/or monitored using several techniques, including satellite-based remote sensing, e.g., with the Total Ozone Mapping Spectrometer (TOMS) (e.g., [6,7]), and the Ozone Monitoring Instrument (OMI) (e.g., [8,9]), MultiGas (Multi-sensor Gas Analizer System) in plumes (e.g., [10]), direct sampling of fumarolic gases (e.g., [2,11]), and ground-based remote techniques, such as the Correlation Spectrometer (COSPEC) (e.g., [12]), Differential Optical Absorption Spectrometer (DOAS) (e.g., [13,14]), Fourier Transformation Infrared Spectrometer (FTIR) (e.g., [15,16]), and Infrared (IR) and Ultraviolet (UV) cameras (e.g., [17,18]); related observations of sulfate in the plume aerosol phase have also been conducted (e.g., [19,20]).

The UV camera technique is based on the principle of ultraviolet light absorption by SO_2 [21], and has been used for volcanological purposes since 2005 [22,23]. The UV camera has a high temporal resolution and allows simultaneous determination of the plume speed, solving two significant error sources in other previous SO_2 flux methodologies [4] associated with the frequency of the data acquisition and the necessity of estimating plume speed by indirect methods (e.g., atmospheric models). In particular, the UV camera is capable of capturing high time-resolution flux data, which when combined with other techniques can be used to: understand flow dynamics in volcanic conduits (e.g., [24,25]); determine mass flow rates models (e.g., [26]); evaluate eruptive periods of a single volcano (e.g., [27]); determine the gas fluxes arising along volcanic zones/arcs (e.g., [10]); correlate degassing and seismological data (e.g., [28,29]; among other applications. Despite the above, and even considering that the UV camera is a relatively simple method for measuring SO_2 emission rates, uptake from the international user community has been somewhat limited up until now, related to the relatively high cost of the equipment. However, the introduction of the low-cost smartphone sensor-based PiCam UV camera [30,31] can be considered as the starting point of a new stage in the applications of UV cameras in volcanology, based on the characteristics of these units, namely: their small size and light weight, which enables easy transportation; user friendly acquisition and post processing software; but, most importantly, their low cost, facilitating the potential for uptake by almost all volcanic gas research groups and volcanic observatories, worldwide.

In spite of several prior measurements of gas emissions from the volcanoes of northern Chile, involving: direct sampling techniques (e.g., [32–35]), studies of aerosols in plumes (e.g., [36]), COSPEC [37], and based on DOAS instrumentation (e.g., [38]), only a few studies to date have been performed using UV cameras, and those cover only six of the thirteen volcanoes with permanent degassing activity. Those volcanoes, running from north to south are: Guallatiri [1]; Irruputuncu [39]; Ollagüe [39]; Putana [40,41]; Lascar [39]; and Lastarria [42] (Figure 1). The objectives of this paper are: (1) to present the first gas flux results obtained using the PiCam UV camera on 7 persistently passive degassing volcanoes in northern Chile; (2) to discuss the main factors that can influence positively and/or negatively the data quality of these UV camera field measurements; and (3) to compare our results with gas flux data from other prior ground-based remote sensing studies. Amongst this, we present the first SO_2 flux measurements from Olca volcano.

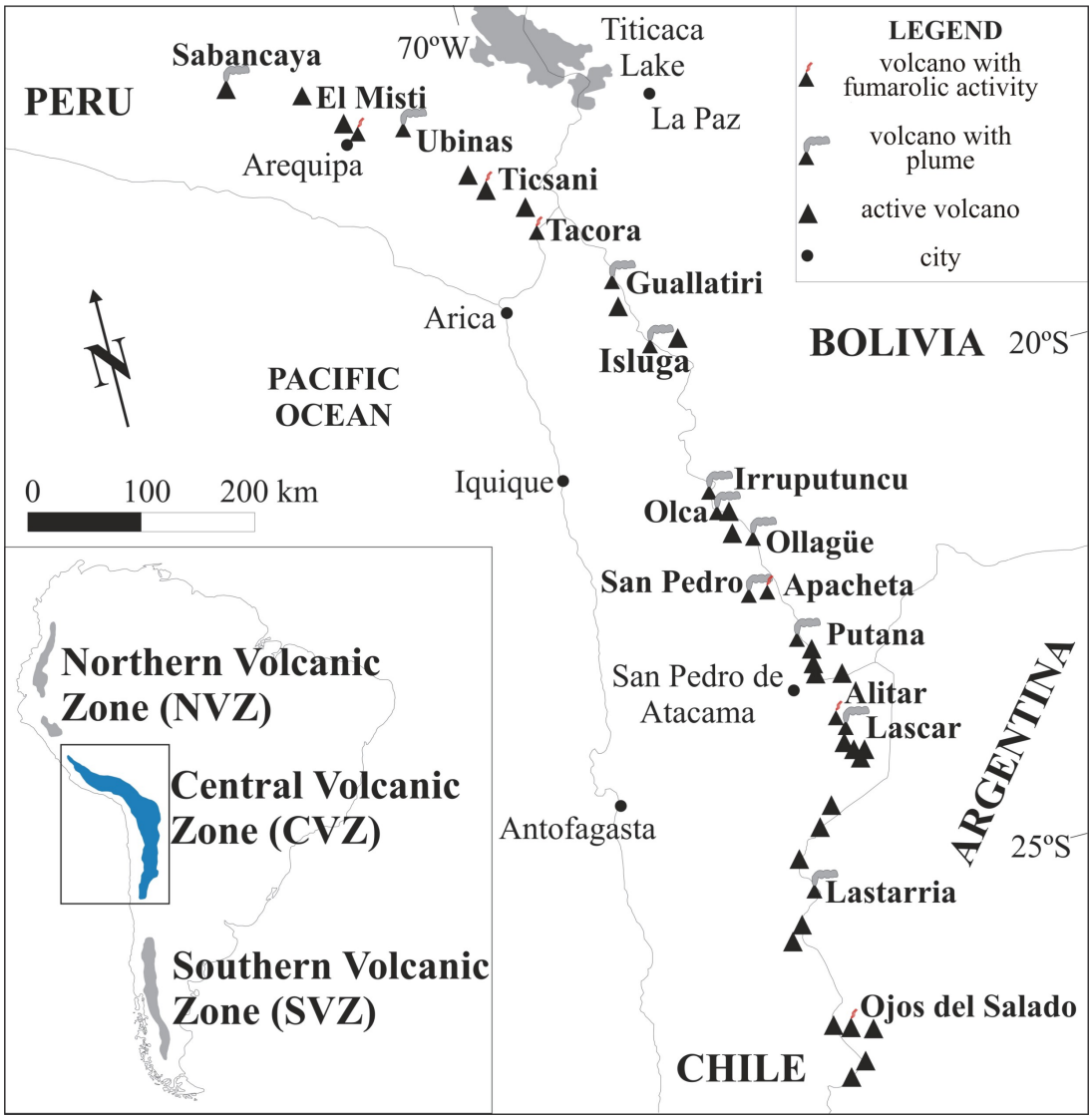

Figure 1. Location map of the Central Volcanic Zone (CVZ) and the position of persistently degassing volcanoes in Chile. Volcanoes with permanent plumes and fumarolic activity are also presented.

2. Geological and Volcanological Settings

2.1. Central Volcanic Zone

The Central Volcanic Zone (CVZ) of the Andes is located between ca. 14° to 27°S, covering southern Peru, western Bolivia, northwestern Argentina and northern Chile (Figure 1). The volcanism in this area is a consequence of subduction of the oceanic Nazca Plate below the continental South American Plate, which is characterized by a convergence rate that ranges between 7.8 and 8.4 cmyr^{-1} [43,44] and an angle of subduction >25° at depths from 100 to 130 km [45]. CVZ is limited by two segments absent of volcanism, to the north by the Peruvian flat-slab (ca. 5°–14°S) and to the south by the Pampean flat-slab (ca. 27°–33°S), both associated with a decrease in the slab subduction angle [46].

CVZ contains more than 40 volcanic centers that have registered eruptive activity in the last ca. 10 ka (e.g., [47–49]. In the case of northern Chile, the active volcanism is present between 17.72°S (Tacora volcano) and 27.12° (Ojos del Salado volcano), and hosts more than half of Holocene actives centers of the CVZ [47–49]. The hyper-arid climate since the Pleistocene has allowed good conservation of volcanic centers [47], characterizing this zone by well-preserved stratocones, cinder cones, and ignimbrite deposits [44]. The basement in the Chilean portion of the CVZ is constituted by

Paleoproterozoic to Late Paleozoic igneous and metamorphic rocks [46,50,51] in a continental crust that reaches >70 km thickness [52,53], affecting the chemistry of volcanic products, through assimilation of this crustal material [54–59].

Volcanic activity has been reported in some detail since the 19th century (e.g., [60]), including documentation of intense fumarolic activity without historical eruptions (Tacora, Guallatiri, Olca, Ollagüe, Apacheta-Aguilucho, Putana, Alitar, Lastarria and Ojos del Salado volcanoes; [33,47–49,60,61], phreatic to phreatomagmatic events with a Volcanic Eruptive Index (VEI) 2 (Isluga, Irruputuncu and San Pedro volcanoes; [48,62,63], and a subplinian eruption of Lascar volcano with a VEI of 4 (19–20 April 1993; [64,65]). Currently, Lascar presents extensive fumarolic activity (e.g., [32]), with sporadic vulcanian events with VEI 2-3 (e.g., [66–70].

2.2. Study Cases

Nine of the thirteen persistently degassing volcanoes in northern Chile exhibit permanent gas plumes (Figure 1), which vary considerably in size and gas concentration. The main characteristics of the seven volcanic systems measured in this work are summarized as follows:

Guallatiri (18°25′S; 69°05′W; 6071 m a.s.l. (meters above sea level)) is a Pleistocene-Holocene volcano, and its geological evolution can be divided into seven stages, which include the emission of thick lava flows, lava domes, pyroclastic flows and fallout deposits, with rock compositions ranging from andesites to dacites [71]). Despite having no records of confirmed eruptive activity, Guallatiri hosts hundreds of fumarolic emissions in two areas, the summit and the southern flank fumarolic fields, which produce two permanent gas plumes: the flank fumarolic field plume is the largest and related to a major fracture network, whilst the smaller summit plume is related to a lava dome from the last stage of evolution [71]. Measured outlet gas-temperatures vary from 82 to 265 °C. Several thermal and cold springs of sulfate to bicarbonate composition appear in the northern, western, and southwestern flanks, where temperatures reach up to 50.1 °C [72].

Isluga (19°09′S; 68°50′W; 5320 m a.s.l.) is a stratovolcano that was built in four stages during the Pleistocene-Holocene, being constituted by lava and pyroclastic flows (with trachy-andesite, trachy-dacite and dacite magmas), and lahar deposits [73,74]. Minor eruptions have occurred during the second half of the 19th and 20th centuries. The last confirmed eruption was in 1913 [60]. Céspedes et al. [63] reported a plume rising 400 m above the crater, a strong sulfur smell in zones close to the volcano, "underground" noises and low intensity seismicity during 2003. Isluga has persistent fumarolic activity, which is limited to its active crater (of ~400 m diameter), and two major fumaroles located in the southern flank, ~100 m below the crater rim. This activity produces a relatively dense single plume, rising to an altitude ranging between 400 and 900 m over the crater.

Irruputuncu (20°43′S; 68°34′W; 5163 m a.s.l.) is a compound volcano with two nested craters, one of them active. Two volcanic edifices form Irruputuncu, the second located in the amphitheater left by the collapse of the southwestern flank of the first edifice. This volcano's volcanic eruptive products include lava flows and domes, pyroclastic flows, block-and-ash flows, and debris avalanche deposits, with andesitic, dacitic, trachy-andesitic, and trachy-dacitic compositions [75]. There is only one report of recent eruptive activity; this pertains to a small phreatic eruption in 1995 [62]. Irruputuncu hosts fumarolic fields in its active crater, and in the outer southern border of this crater [76]. Fumarolic emissions have variable outlet temperatures, ranging between 83 °C and 240 °C, with high concentrations of CO_2 and SO_2 suggesting a magmatically-dominated system [33]. The vigorous fumarolic activity causes a single plume that reaches up to ~200 m over the summit [76]. Additionally, several thermal springs are located in its west flank, with temperatures that reach up to 33 °C.

Olca (20°57′S; 68°30′W; 5450 m a.s.l.) is part of a 20 km long east–west oriented volcanic chain called Olca-Paruma [47], which is constituted by a series of overlapping stratovolcanoes, from west to east: Michincha, Olca, Cumbre Blanca, Candelaria, and Paruma, respectively [77,78]. The geological evolution of the chain is highly complex, and includes Upper Pleistocene-to-Holocene eruptive products including lava flows, lava domes and pyroclastic flows of andesitic-to-dacitic compositions [48,51,78].

Olca presents persistent fumarolic activity, which is related to formation of a lava dome, which arose in the last eruptive episode [76]. Fumarole outlet temperatures vary between 84 °C and 91 °C, and the gas composition is dominated by hydrothermal components [33]. The fumaroles produce a very discrete single gas plume, with an average altitude of ~50 m over the dome. There are no records of historical eruptive activity.

Ollagüe (21°18'S-68°11'W; 5868 m a.s.l.) is a composite stratovolcano situated 12 km southeast of Ollagüe village (~300 inhabitants). Ollagüe volcano summit hosts, in its outer southwestern side, permanent fumarolic emissions, which are related to a lava dome/flow and produce a single gas plume that rises up to 300–600 m over the summit. Ollagüe volcano has a multistage eruptive history, including rhyodacitic domes, silicic andesitic-to-dacitic lava flows and domes, pyroclastic flow and surge and block-and-ash flow deposits [44]. There are no records of historical eruptive activity.

San Pedro (21°53'S; 68°24'W; 6145 m a.s.l.) is a compound stratovolcano located 85 km northeast from Calama city and is part of the NW-SE trending volcanic chain San Pedro-Linzor (SPL; [79]) and of a short E–W chain formed by San Pablo and San Pedro volcanoes and La Poruña scoria cone [80]. San Pedro volcano is formed by two cones, with an estimated combined volume of 140 km^3. San Pedro was built in four stages, and is constituted of lava flows and domes, several scoria and pumice pyroclastic deposits (pyroclastic flow and fallout deposits) and debris avalanche deposits [81,82], with basaltic andesite, andesite, and dacite compositions. Persistent fumarolic activity is present in the upper part of the younger cone nested in the border of a lava flow, producing a discrete single gas plume reaching up to ~200 m over the crater. The historical activity includes more than ten events from the 1870s [83,84] and Martin [85] details an eruption which occurred in 1901, causing considerable damages to local infrastructure.

Putana (22°34'S–67°52'W; 5890 m a.s.l.) is located on the border between Chile and Bolivia, and is a stratovolcano with a relatively well-preserved summit crater, several satellite vents and a number of post-glacial eruptive features [47,48]. The edifice consists of several sequences of basaltic andesites, andesitic and dacitic lava flows-and-domes and pyroclastic deposits [47,48,86]. Putana volcano presents four active fumarolic fields in the summit crater area, related to a small crater and lava flows. Fumarole outlet temperatures vary from 82 to 88 °C and chemical compositions reflect two sources of fluids (magmatic and hydrothermal; [33]). The fumarolic activity produces a 100–500 m height plume [33], although it is very common to observe distinct plumes related to each individual fumarolic field. There are no records of historical eruptive activity.

3. Methodology

3.1. PiCam UV Camera

The PiCam is a low-cost SO_2 UV camera, based on two modified Raspberry Pi v1 camera modules. Each camera sensor (Omnivision OV5647) was modified using the technique described in Wilkes et al. [30], by chemical removal of the sensor's Bayer filter. This vastly increases the detector's responsivity to UV radiation and removes the mosaic pattern response imposed by the Bayer filter. The optical system was built (following Wilkes et al. [30,31]) around these detectors using 3D printed lens holders and an off-the-shelf plano-convex lenses (9 mm focal length, 6 mm diameter; Edmund Optics Inc.). These modules were co-aligned, with an overall system field-of-view of 23.1° × 17.3° (width × height). A 10 nm full width and half maximum bandpass filter (Edmund Optics Inc.) was mounted to the fore of each lens, with peak transmissions wavelengths of 310 nm (Filter A) and 330 nm (Filter B) respectively, corresponding to spectral regions where SO_2 does, and does not absorb UV light (e.g., [22]).

The cameras were connected to Raspberry Pi 3 Model B computers for interfacing, all housed within a PeliCase instrument case along with a battery and GPS (Global Positioning System) for timestamping the acquisitions. A Windows laptop was used to communicate with the Raspberry Pi wirelessly, controlling data capture via custom Python 3 code.

Image processing was achieved by contrasting the 310 nm and 330 nm channels to isolate the SO_2 absorption, then calibrating these images via gas cell calibration (e.g., [22,87]). The applied cells contained column densities of 100, 467, and 1989 (all ±10%) ppm·m, and in all cases the calculated apparent absorbances and column densities displayed a good linear fit (Figure 2); furthermore, all measured field column densities presented herein were below 1989 ppm·m; therefore, falling within the range in which the calibrations were valid.

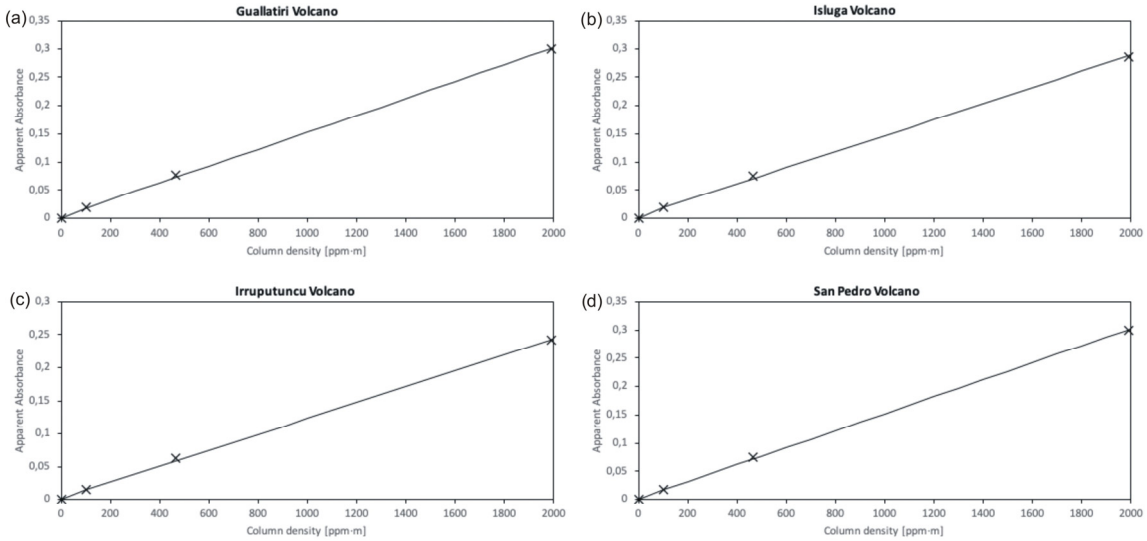

Figure 2. Calibration plot showing the column densities from gas cell calibration [ppm·m] vs. apparent absorbance of the (**a**) Gualltiri, (**b**) Isluga, (**c**) Irruputuncu, and (**d**) San Pedro volcanoes.

3.2. Fieldwork

Here we present data from four field campaigns, which were carried out during November 2017, December 2017, February–March 2018, and April 2018. The details of the measurements from each site are summarized below (see also Table 1; Supplementary Material Figure S1):

Table 1. Table with all technical details of the measurements; m a.s.l.: Meters above sea level. * Local Table from May to August; UTC-3 from September to April). (1) OCV: OpenCV post processing method, CP: Control Points post processing method. (2) Measurements from images do not align correctly in OCV method. n.d. Not determined, n.r.d. Not reliable data.

Volcano	Date	Site	Coordinates		Altitud (m a.s.l.)	Distance from the Plume (km)	Measure Sequence	Time			Shutter Speed		Framerate (Hz)	Images		Proccesing Methods (1)	Plume Speed OCV (ms^{-1})	SO_2 Emission Rate OCV (td^{-1})			Plume Speed CP (ms^{-1})	SO_2 Emission Rate CP (td^{-1})		
			Lat	Long				Starting *	Ending *	Span (min)	Filter A	Filter B		Captured	Proccessed			Average ± 1	Minimum	Maximum		Average ± 1	Minimum	Maximum
Guallatiri	10 December 2017	1	−18.466677	−69.110220	4658	5.2	1	11:00	11:55	55	700	100	0.25	1555	1064	CP	n.d.	n.d.	n.d.	n.d.	9.0	49.4 ± 18.8	13	101
	12 December 2017	2	−18.459761	−69.168300	4305	10.8	1	11:37	12:22	45	600	100	0.2	1070	492	OCV	10.3	50.5 ± 12.3	19.9	86.4	n.d.	n.d.	n.d.	n.d.
	13 December 2017	3	−18.390355	−69.120780	4933	4.8	1	11:26	12:16	50	80	11	0.2	1156	1156	OCV/CP	n.r.d.	n.r.d.	n.r.d.	n.r.d	n.r.d.	n.r.d.	n.r.d.	n.r.d
	5 April 2018	4	−18.483295	−69.140873	4315	8.4	1	11:38	12:22	44	200	50	0.2	1062	1062	CP	n.d.	n.d.	n.d.	n.d.	1.0	5.5 ± 2.8	1.7	13
							2	12:29	13:14	45				1084	1084	OCV	2.2	12.2 ± 3.1	4.3	19.9	n.d.	n.d.	n.d.	n.d.
							3	13:21	14:06	45				1068	320	CP	n.d.	n.d.	n.d.	n.d.	8.5	19.1 ± 4.5	10.4	32
							4	14:11	14:42	31				744	744	OCV	9.3	28 ± 9.3	9.5	51	n.d.	n.d.	n.d.	n.d.
Isluga	4 April 2018	1	−19.203115	−68.865454	4103	6.2	1	11:05	11:49	44	350	70	0.2	1046	644	CP	n.d.	n.d.	n.d.	n.d.	10.9	329 ± 90.8	177	569
							2	11:55	12:08	13				312	312	OCV	10.4	199 ± 47.5	129	325	n.d.	n.d.	n.d.	n.d.
							3	12:18	12:40	22				505	504	OCV/CP	n.r.d.	n.r.d.	n.r.d.	n.r.d	n.r.d.	n.r.d.	n.r.d.	n.r.d
							4	12:45	13:30	45				1072	1072	OCV	13.1	361 ± 31.6	285	495	n.d.	n.d.	n.d.	n.d.
							5	13:38	14:05	27				630	630	CP	n.d.	n.d.	n.d.	n.d.	7.0	129 ± 28.3	58.8	206
Irruputuncu	2 April 2018	1	−20.760319	−68.572877	4182	3.3	1	12:57	13:40	43	350	75	0.2	1058	1058	OCV/CP	6.0 (2)	86.6 ± 11.1 (2)	60.5	114.9	5.9	56 ± 10	31.1	80.4
							2	13:47	14:29	42				964	964	CP	n.d.	n.d.	n.d.	n.d.	5.3	40.2 ± 6.2	19	54.4
							3	14:32	15:16	44				1050	554	CP	n.d.	n.d.	n.d.	n.d.	3.9	22.3 ± 5.3	10.4	35.4
	3 April 2018						1	10:15	10:55	40	350	50		946	949	CP	n.d.	n.d.	n.d.	n.d.	4.8	21.4 ± 5.5	12.1	38
							2	11:11	11:51	40	350	60		960	960	CP	n.d.	n.d.	n.d.	n.d.	2.6	25.4 ± 3.1	17.3	32.8
							3	11:58	12:38	40				954	656	CP	n.d.	n.d.	n.d.	n.d.	4.4	16.5 ± 5.4	3.5	30.2
Olca	1 March 2018	1	−20.944073	−68.478082	5300	0.6	1	12:45	12:50	5	55	10	0.2	130	130	OCV	0.9	n.r.d.	n.r.d.	n.r.d	n.d.	n.d.	n.d.	n.d.
							2	12:58	13:29	31	55	10		742	742	OCV	9.1	18.4 ± 13.4	0	58.4	n.d.	n.d.	n.d.	n.d.
							3	13:52	14:23	31	100	15		732	732	OCV/CP	n.r.d.	n.r.d.	n.r.d.	n.r.d	1.0	n.r.d.	n.r.d.	n.r.d
Ollagüe	1 March 2018	1	−21.280380	−68.233636	4012	5.9	1	17:13	17:55	42	230	40	0.2	1012	786	OCV/CP	8.4	15.9 ± 3.1	7.5	25	9.4	7.9 ± 2.1	2.6	16.4
							2	18:16	18:47	31	220	35		738	448	OCV/CP	7.4	19.2 ± 4.1	8.3	34.2	n.r.d.	n.r.d.	n.r.d.	n.r.d

Table 1. *Cont.*

Volcano	Date	Site	Coordinates		Altitud (m a.s.l.)	Distance from the Plume (km)	Measure Sequence	Time			Shutter Speed		Framerate (Hz)	Images		Proccesing Methods (1)	Plume Speed OCV (ms^{-1})	SO_2 Emission Rate OCV (td^{-1})			Plume Speed CP (ms^{-1})	SO_2 Emission Rate CP (td^{-1})		
			Lat	Long				Starting *	Ending *	Span (min)	Filter A	Filter B		Captured	Proccessed			Average ± 1	Minimum	Maximum		Average ± 1	Minimum	Maximum
	2 March 2018	2	−21.272022	−68.231213	3958	6.3	1	9:48	10:23	35	180	45	0.2	836	836	OCV/CP	9.5 (2)	92.5 ± 14.4 (2)	63.1	139.1	3.7	21.5 ± 4.0	13.8	38
							2	10:44	11:26	42	160	40		1008	1008	OCV/CP	3.7	5.8 ± 4.6	0.8	28.4	3.3	4.8 ± 2.0	0.9	12.1
							3	11:44	11:52	8	65	5		188	188	OCV/CP	n.r.d.	n.r.d.	n.r.d.	n.r.d	n.r.d.	n.r.d.	n.r.d.	n.r.d
San Pedro	28 February 2018	1	−21.835503	−68.370719	4350	6	1	11:45	12:40	55	230	30	0.2	1324	350	OCV/CP	6.8	7.4 ± 1.6	3.6	11.2	n.r.d.	n.r.d.	n.r.d.	n.r.d
							2	12:59	13:55	56				1332	746	OCV/CP	12.9	16.2 ± 6.5	5.2	43.2	7.6	16.1 ± 4.6	6.9	32
Putana	29 November 2017	1	−22.585581	−67.895600	4935	5.3	1	10:40	11:20	20	600	75	0.25	560	560	OCV	6.1	31.9 ± 9.8	7.6	66.8	n.d.	n.d.	n.d.	n.d.
	9 March 2018	2	−22.548809	−22.548809	4467	9.5	1	12:29	12:44	15	500	100	0.2	360	360	OCV/CP	5.1	5.6 ± 1.4	3.5	11.2	5.0	6.1 ± 1.4	4.2	14.2
							2	12:53	13:08	15				356	356	OCV/CP	4.5	5.5 ± 1.4	3.5	11.2	8.0	4.8 ± 2	0.9	13
							3	13:16	13:30	14	720	125	0.25	402	402	OCV/CP	6.2	11.9 ± 3.1	6.9	24.2	6.3	9.8 ± 2.8	6	19
							4	13:48	14:02	14	700	100	0.2	348	348	OCV/CP	6.8	4 ± 1.1	1.7	8.6	6.8	3.2 ± 1	1.7	7.8
							5	14:06	14:32	26				628	628	OCV/CP	5.2	2.8 ± 1.6	0.9	9.5	5.6	3.9 ± 1.3	1.7	14.2

In Guallatiri, volcano measurements were performed during the 10, 12, and 13 December 2017, and 5 April 2018 from 4 points located between 4.8 and 10.8 km from the summit plume, at altitudes varying from 4305 to 4933 m a.s.l. A total of 7 measurement sequences were captured between 11:00 and 14:42 hrs local time (UTC-3), with time spans ranging 31–55 min. Shutter speed for filters A and B varied from 80 to 700 ms, and 11 to 100 ms, respectively, and the image capture frequency of the cameras was set to 0.2–0.25 Hz, providing images every 4 and 5 seconds.

Measurements in San Pedro, Olca, and Isluga volcanoes were performed during 28 February, 1 March, and 4 April 2018, respectively. The observations were carried out in locations 6, 0.6, and 6.2 km (at 4103; 5300; 4350 m a.s.l., respectively) from the plume source. For Isluga volcano, five measurement sequences were performed, whereas for Olca and San Pedro volcanoes, three and two image sequences, respectively, were acquired, with acquisitions between 11:05 and 14:23 hrs local time, lasting from 5 to 56 min. In this case, shutter speeds for filter A were between 55 and 350 ms, and for filter B, between 10 and 70 ms, with an image capture frequency of 0.2 Hz.

Two days of measurements were carried out in *Putana* (29 November, 2017 and 9 March, 2018), Ollagüe (1 and 2 March, 2018) and Irruputuncu (2 and 3 April, 2018) volcanoes. Two sites each were used for Ollagüe and Putana volcanoes, in the first case 5.9 and 6.3 km, respectively from the summit fumarolic field, and in the latter case 5.3 and 9.5 km from the plume source, with site altitudes that varied between 3965 and 4935 m a.s.l. In the case of Irruputuncu, all measurements were carried out from the same point, located 3.3 km from the active crater, at 4182 m a.s.l. Six measurement sequences were acquired at Irruputuncu and Putana, whereas five were captured at Ollagüe, between 9:48 and 18:47 hrs local time, spanning between 8 and 44 min in duration. In these cases shutter speeds for filter A were set between 65 and 600 ms, and for filter B, between 5 and 100 ms, and the image capture frequency ranged from 0.2 and 0.25 Hz.

3.3. Post Processing

Image processing was performed post-acquisition, using a custom written Python 3 code; for a comprehensive description of the range of processing techniques for determining SO_2 fluxes from UV cameras please see Gliß et al. [88]. Here, processing followed the protocols outlined by Kantzas et al. [87]. Image registration, in order to ensure co-alignment the images from each of the camera channels, was performed via two methods:

(i) automated registration using the findTransformECC function of the OpenCV library (OCV). This finds the optimum image transformation with respect to the enhanced correlation coefficient (ECC) criterion with a Euclidean model; the off-band camera images can then be warped by this tranformation using the warpPerspective() function;

(ii) manual control point selection (CP) registration allows manual mapping of points in one scene to those in another, and an optimal affine transformation is then generated to best fit these points. This uses the scikit-image python module, through a SimilarityTransform() object.

The OCV is a fast method that allows a first estimate of the plume speed and SO_2 rates retrieved from a single volcano. The performance of the two methods is assessed later.

Other processing steps included: all the captured images were dark image corrected; image vignetting was corrected using a clear-sky mask image acquired in the field; furthermore, the clear-sky background intensity was determined by averaging the pixel intensities in a region of the clear sky close to the plume; finally, plume speeds were calculated using the cross-correlation technique (e.g., [22]).

The PiCams' sensitivity to SO_2 has been shown to vary by up to 15% between the center of the image and the extreme edge of the field of view [31], due to changing filter transmission characteristics with changing illumination angle. Therefore, in order to avoid major differences in the measurements across the field-of-view of the PiCam, we placed the plume in the middle of the image and extracted column densities across a cross-section through the plume, which was generally quite central to the image (as showed in the Supplementary Material Figure S2). Therefore, we can anticipate it would not change more than 5% for the cross sections used to extract plume column densities.

3.4. Estimation of the PiCam UV Camera Uncertainties

Several uncertainties can affect the quality of the data, and their review is necessary in order to estimate the total uncertainty of the measurements. We determined possible sources of errors, which include the plume speed, which depends on plume distance and time uncertainty, gas cell column densities, calibration drift, light dilution, SO_2 detection, plume direction, and multiple scattering. We estimated the errors using our data, information available in the literature (especially information available from the studied zones) and field protocols, the last applied to minimize possible sources of errors, as mentioned previously.

The plume speed uncertainty depends directly on the time uncertainty associated with the difference in time of the plume movement between the two integrated columns amounts (ICA) during cross-correlation, and from the plume distance uncertainty (which translates to an uncertainty associated with the distance between the two ICA); for the latter we considered distance errors of 50, 100 and 200 m. The plume speed uncertainty is controlled mostly by the time uncertainty, which varies in our measurements from 8.3 and 25%, whereas in the case of the plume distance error, independently variation between 50 and 200 m, this is <3.8%, with the exception of Guallatiri, Irruputuncu and Olca, where maximum errors were 4.2, 6.1, and 17%, respectively (Table 2). In consequence, we obtained a plume speed error range from 5.9 to 18% (Table 2).

Table 2. A list of sources of errors (uncertainties) and its respective values. The total root mean square (RMS) error is also reported. The higher error in the positive error reported in the total RMS correspond to the underestimation related to the light dilution. (-) negligible error, (*) maximum error considering the maximum light dilution for volcanoes measured in distances >8 km.

Uncertainty		Volcano						
		Guallatiri	**Isluga**	**Irruputuncu**	**Olca**	**Ollagüe**	**San Pedro**	**Putana**
Plume Distance	min	±0.4	±0.8	±1.5	±0.3	±0.8	±0.8	±0.5
	max	±4.2	±3.2	±6.1	±17	±3.4	±3.3	±3.8
Time	min	±8.3	±8.3	±8.3	±8.3	±13	±8.3	±8.3
	max	±13	±13	±13	±13	±17	25	±13
Plume Speed	min	±5.9	±5.9	±6	±5.9	±8.9	±5.9	±5.9
	max	±9.3	±9.1	±9.8	±15	±12	±18	±9.2
Gas Cell Calibration		±10	±10	±10	±10	±10	±10	±10
Calibration Drift	min	±0.8	±2.3	±0.4	±5.1	±7.5	±1.1	±7.2
	max	±3.5	±9.5	±15	±15	±19	±2.8	±19
Light Dilution	min	+20	+20	+20	+20	+20	+20	+20
	max	+42						+42
SO_2 detection		±15	±15	±15	±15	±15	±15	±15
Plume Direction		±5	±5	±5	±5	±5	±5	±5
Multiple Scattering		-	-	-	-	-	-	-
Total RMS Error	min	−8.7/+11	−8.7/+11	−8.7/+11	−9/+8.2	−9.8/+12	−8.7/+11	−9.3/+12
	max	−9.4/+19	−10/+12	−12/+13	−12/+11	−12/+14	−12/+12	−13/+21
	max (*)	+12						+14

Another source of error can be related to the differences between the calibrations throughout the day, due to changes in the sun position and in consequence, changes in the illumination of the background. The calibration process depends directly on the gas cells concentration, which have an error of 10% (manufacturer quoted), and as mentioned previously, of the sun position and its incidence in the camera. We calculated the calibration drift error comparing two consecutive calibrations in all sites measured and considering all the calibrations done in a single day. This error varies widely

between 0.4 and 15%, whereas in the case of Ollagüe volcano it reached up to 19%, which is explained by one calibration being performed in a different site from where measurements were performed, in fact, more than 50 km of distance, consequently, with very different illumination conditions.

Light dilution, caused by scattering of photons into the FOV (Field of View) of the camera between the plume and the instrument, can have a considerable effect on measured emission rates, with Campion et al. [89] demonstrating that it can cause underestimation of up to 80%. This effect is dependent on atmospheric conditions, such as pressure, humidity and aerosol concentration, SO_2 concentration and distance of the measuring point from the plume. In the case of northern Chile volcanoes, where summit craters are located at altitudes over 5000 m a.s.l., the zone is characterized by a thin atmosphere and a very dry environment, where the dilution effect is more reduced. Lopez et al. [42] reported SO_2 emission rates from Lastarria volcano (northern Chile), where measurements were made at an altitude ~4500 m a.s.l. and 7 km distance from the plume, estimating a light dilution in a range of 50–60%. Similarly, Stebel et al. [41] determined uncertainty of 25–30% for UV camera measurements carried out in Putana volcano (measuring point at ~4900 m a.s.l. and 6 km from the plume), where light dilution is included. Llanko et al. [90], using two UV cameras simultaneously, found that at Sabancaya volcano (southern Peru) measurements performed 4.25 km from the active vent incorporated an underestimation of 50% due to light dilution. In order to have a general approach to light dilution effect in our measurements, we performed measurements in Guallatiri volcano at several distances from the gas plume sources (between 4.8 and 9.5 km from the gas plume source; Table 1). Despite all measurements being performed at different periods of time, they were carried out under broadly similar atmospheric conditions. Additionally, degassing has been constant in the last century and absent of eruptive activity in that period, and we compare exclusively measurements with similar plume speeds (a maximum difference of ±0.5 ms^{-1}). In this case, measurements carried out 5.2 km from the summit plume, and plume speed 9 ms^{-1}, gave SO_2 rate average for a whole sequence of 49.4 ± 18.8 td^{-1}, whereas at 8.4 km distance, plume speeds of 8.5 and 9.3 ms^{-1}, SO_2 rates averaged 19.1 ± 4.5 and 28 ± 9.3 td^{-1}, respectively (Table 1). Assuming these differences in SO_2 emission rates are due exclusively to the light dilution effect, this effect could be causing an underestimation in our measurements of ~42% less than the original SO_2 rate for measurements carried out at long distances (>8 km) from the gas plume sources (Figure 3). In consequence, for measurements made <3 km from the plume we anticipate that light dilution will be negligible (Figure 3), whilst our measurements at >3000 m distance may be underestimating at least by 20% up to 6 km distance. Due to snow being present on a number of the volcano flanks during measurements, using Campion et al.'s [89] light dilution correction was not possible.

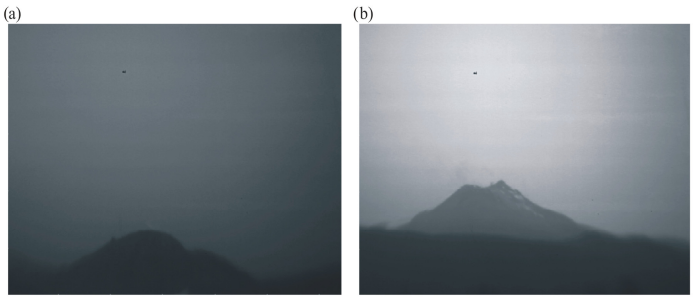

Figure 3. (**a**) Absorbance image from Olca volcano with negligible effect from light dilution (note that volcanic edifice appears completely black), which was taken from 0.6 km from the gas source; (**b**) absorbance image from Guallatiri volcano affected by light dilution (note that volcanic edifice in the background appears light gray, whereas in the foreground the outcrops appear completely black), which was taken from 10.8 km from the gas source.

The uncertainty relating to SO_2 detection depends on the sensor noise and the sensitivity of the system to SO_2 [18]. Wilkes et al. [31] found this uncertainty to be 3–4% for the PiCam during

tests on Etna when measuring a strong plume. However, this used a detection limit estimated based on a significantly undersaturated sensor. Whilst plumes measured in this work were smaller, high image intensities were ensured by modifying shutter speeds appropriately, to minimize sensor noise. We therefore estimate that the uncertainty associated with this should not exceed 15%.

Klein et al. [91] discuss the effects of the angle between the viewing direction and the plume motion, where measurements perpendicular to the plume up to 40° should not to produce major differences in the SO_2 emission rates, but producing errors up to 50% at more acute angles. Additionally, the variation of the angle can be produced by changes in the wind direction and consequently in the plume during the measurements. The majority of our measurements were carried out viewing perpendicular to the plume motion, except for Ollagüe, San Pedro and 1 sequence from Putana volcano, in all cases with angles less than 40°. Our measurement sequences lasted for a maximum of 56 minutes, reducing the chances to variations in the propagation angle of the plume within an image sequence. Since no changes in the plume propagation were observed in any sequence measured, we assumed a maximum of 5% error due to this process (Table 2). Multiple scattering is produced by presence of abundant condensed aerosol in the plume, which could produce errors in the SO_2 flux retrieved by changing photon paths through the plume. All of our measured plumes were very transparent, suggesting a very low content of condensed aerosol in the plume; consequently, we assume that the error related to multiple scattering is negligible.

The total root mean square (RMS) error estimated for all volcanoes measured varies in a range of 8.7 and 14% (Table 2). In the cases where errors can be obtained with minimum and maximum values, we presented both values, consequently, minimum and maximum errors were also calculated (Table 2). In the cases of Guallatiri and Putana volcanoes, where some measurements were done in a distance over 8 km from the plume, errors including high underestimations due light dilution were also calculated, producing higher total RMS error, up to 19 and 21%, respectively (Table 2).

4. Results

Results from each volcano are presented in Table 1 and are summarized as follows (processed images from each volcano are also presented in Supplementary Material Figure S2):

From Guallatiri volcano 7739 images were acquired, and 5922 images were processed. Images that are not processed, due to shaking of the PiCam during the field measuring producing errors in the plume speed calculation and/or SO_2 emission rates, will be discussed in the following sections. The determined plume speed ranged 1.0 to 10.3 ms^{-1}. Of the three image sequences from the December 2017 fieldwork, two provided reliable flux data (considering not reliable data when cross correlation technique did not work to obtain the plume speed or post processing methods can not retrieve emission rates), where the averages ± one standard deviation (1σ) of the SO_2 emission rate were 49.4 ± 18.8 and 50.5 ± 12.3 td^{-1} for the 10 and 12 December, 2017, respectively, whereas from the four sequences acquired during 5 April, 2018, the emission rates were 5.5 ± 2.8, 12.2 ± 3.1, 19.1 ± 4.5, and 28 ± 9.3 td^{-1}, respectively. The maximum rate was captured during 12 December, 2017: 101 td^{-1}. The overall average SO_2 outputs from the December 2017 and April 2018 measurements were 49.8 ± 17.1 and 19 ± 17.7 td^{-1}, respectively, and that across both periods was 29.1 ± 22.6 td^{-1}. The emission rates pertain to degassing from the gas plume from the summit fumarolic field, due to post processing for southern flank fumarolic field producing no reliable data.

A total of 3565 images were obtained during the one day of measurements from Isluga volcano, with 5 sequences acquired and all the images were processed, such that reliable fluxed were determined from all sequences, barring sequence 3. The determined plume speeds varied between 7.0 and 13.1 ms^{-1} and the SO_2 emission rates for sequences 1, 2, 4, and 5 were 329 ± 90.8, 199 ± 47.5, 361 ± 31.6 and 129 ± 28.3 td^{-1}, respectively, with an overall average of 254 ± 49.6 td^{-1}. The maximum SO_2 emission rate was measured in sequence 1:569 td^{-1}.

In the case of Irruputuncu volcano, 6 sequences were acquired, involving a total of 5932 images, of which 5141 images were processed, obtaining reliable data in all sequences. The resolved plume

speed varied from 2.6 to 5.9 ms^{-1}, and SO_2 emission rates averaged for individual sequences varied from 16.5 ± 5.4 to 56 ± 10 td^{-1}, with higher rates measured during the first day (22.3 ± 5.3-56 ± 10 td^{-1}; 2 April, 2018) than the second (16.5 ± 5.4–25.4 ± 3.1 td^{-1}; 3 April, 2018). The highest SO_2 rate was measured during sequence 1, day 1, reaching up to 80.4 td^{-1}. The overall SO_2 output for 2 April was 39.5 ± 7.2 td^{-1} and 3 April, 21.1 ± 4.7 td^{-1}, averaging 30.3 ± 6 td^{-1} across both days.

At Olca and San Pedro volcanoes, 3 and 2 sequences were acquired, with 1604 and 2656 images, respectively. All the Olca images were processed, whereas only 1096 images from San Pedro were processed. It was not possible to acquire reliable gas fluxes from sequence 1 from Olca volcano. A wide range of plume speeds were measured, varying from 0.9 to 9.1 ms^{-1}. In spite of it being possible to determine plume speed in sequences 1 and 3 for Olca volcano, the resulting SO_2 emission rates were close to zero, being here considered as a not reliable data, whereas for sequence 2 the average measured rate was 18.4 ± 13.4 td^{-1}, with a maximum of 58.4 td^{-1}. Plume speeds measured for San Pedro volcano varied from 6.8 to 12.9 ms^{-1}. The average SO_2 emissions rates ranged between 7.4 ± 1.6 and 16.2 ± 6.5 td^{-1}, with a maximum rate of 43.2 td^{-1} and an overall average SO_2 output of 13.2 ± 4.2 td^{-1}.

Flux data were obtainable from 4 of the 5 acquired sequences from Ollagüe volcano, whereby 3266 of the 3440 captured images were processed. The plume speed values ranged between 7.4 and 9.4 ms^{-1}, on 1 March 2018, and between 3.3 and 3.7 ms^{-1} on the 2 March, 2018. Measurements on the first day were carried out during the afternoon, when the wind speed normally increases, whereas the second day's measurements were performed during the morning. Average SO_2 emission rates during 1 March varied from 7.9 ± 2.1 to 19.2 ± 4.1 td^{-1}, and those during 2 March between 4.8 ± 2 and 21.5 ± 4.0 td^{-1}. The overall SO_2 output for the first and second days were 14.3 ± 3.1 and 10.7 ± 3.5 td^{-1}, respectively, and that averaged over the whole period was 12.5 ± 3.3 td^{-1}; the maximum rate of 38 td^{-1} was measured on 2 March.

From Putana volcano 2654 images were obtained and processed. Plume speeds ranged from 4.5 to 8.0 ms^{-1}. SO_2 emission rates obtained during 29 November, 2017 averaged 31.9 ± 9.8 td^{-1}, with a maximum of 66.8 td^{-1}, whereas measurements during 9 March, 2018 had sequence averages ranging 2.8 ± 1.6 to 11.9 ± 3.1 td^{-1}, with the maximum rate of 24.2 td^{-1} obtained in the sequence 3. The overall average SO_2 output for 9 March was 5.8 ± 1.7 td^{-1} and for both days was 8.2 ± 2.4 td^{-1}. Despite there being several small plumes emitted from Putana volcano's summit, only the southernmost plume was processed, as it was not possible to obtain reliable data from the central and northernmost plumes.

5. Discussions

5.1. External/Internal Effects during Measuring and Post Processing Methods Comparison

Several effects and capabilities were observed during the data acquisition and post processing, which depends on the external/internal factors and PiCam processing code properties. Camera shake is one of the most important external factors that can affect the PiCam UV camera measurements, influencing during the data acquisition and post processing. Lateral movement of the camera in the field due to wind gusts, generates displacement and blurring of the acquired images. The movement can be verified by checking the sequence producing stop motion videos, where movement of the sequence can be detected (Supplementary Material Figure S3). We observed that if a complete sequence is partially affected by the camera shake is processed, SO_2 emission rates can be under or overestimated, or the plume speed cannot be determined, and consequently, SO_2 emissions rates cannot be retrieved. In this case, we applied an extraction of the displaced/unfocussed images, in order to avoid errors related to the movement of the integrated column amounts (ICA's). Alternatively, future work on more secure tripod mounting, or the use of video stabilization, could provide solutions, which prevent the loss of data. Here we show two cases where improvements can be made using corrected wind-affected measuring sequences:

(1) Sequence 3 from Guallatiri volcano carried out during 5 April 2018 between 13:21 and 14:06 hrs local time (Table 1) produced 1068 images, which only 320 images were not affected by the camera

shake. The processing of the whole sequence was not able to obtain plume speed, and consequently, the retrieval of the SO_2 rates. After removing the camera shake-affected images (748 images), a plume speed of 8.5 ms^{-1} and an average SO_2 emission rate of 19.1 ± 14.5 td^{-1} were obtained for the summit plume, with measured minimum and maximum rates of 10.4 and 32 td^{-1}, respectively.

(2) Sequence 1 from Isluga volcano was acquired 4 April 2018, for 44 minutes starting at 11:05 hrs local time; 1062 images were obtained (Table 1). The whole sequence was processed obtaining a plume speed of 8.6 ms^{-1}, whereas the average SO_2 emission rate was 177 ± 60.7 td^{-1}, with a maximum rate of 387 td^{-1} (Figure 4a). We detected 322 images not camera shake-affected, which were reprocessed (Figure 4b). The new data obtained was a plume speed of 10.9 ms^{-1}, an average SO_2 emission rate of 329 ± 90.1 td^{-1} and a maximum rate of 569 td^{-1}. The comparison between the original and the reprocessed sequences (Figure 5) shows that the extraction of the camera shake-affected images does not produce changes in the general pattern of emission rates, which means that the small-scale shifts in ICA placement are not causing dramatic changes to the observed trends, but an increase in the SO_2 emission rates is produced once camera shake is removed, due to the associated increase in plume speed estimation.

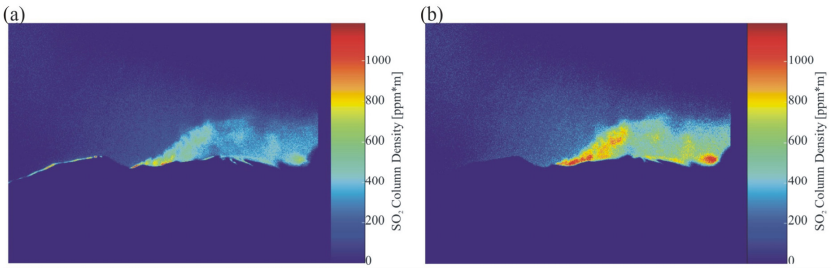

Figure 4. (**a**) Example of an image from a processed sequence affected by camera shake. Note the line showing high SO_2 column density amounts in the left border of the volcano; (**b**) example of an image from a sequence corrected by camera shake. Note the increasing of the high SO_2 column density amounts in the plume in comparison with the Figure 2a.

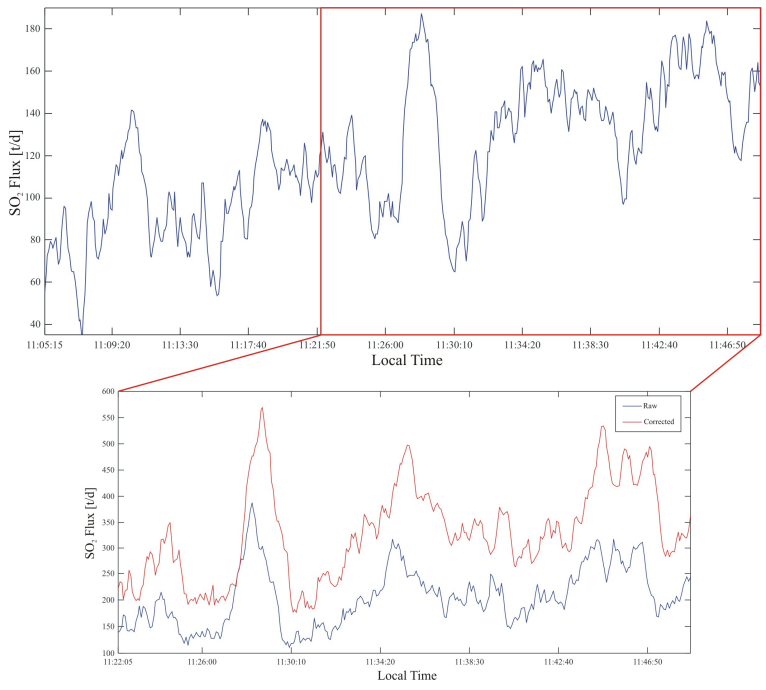

Figure 5. Raw data of the sequence 1 from Isluga volcano (4 April 2018) affected partially by camera shake. The zoom shows the reprocessed data after extracting wind blows affected images, and compared with the same section from the raw data.

The extraction of the displaced/blurred images allows us to obtain information of plume speed and SO_2 emission rates from sequences where we are not able to calculate both parameters due to camera shake. In the cases where plume speed and SO_2 rates are retrieved, the camera shake-affected images extraction process allows us to detect an increasing of plume speed up to 21%, whereas in the case of the SO_2 emission rates these values increase up to 46% over the raw not corrected rates.

Light dilution is another external factor that can influence the final SO_2 emission rates at a single volcano, as discussed in Section 3.4. Campion et al. [89] demonstrated that changes in the atmospheric conditions can produce variations in the light dilution effect, despite light dilution having a high dependence on the distance of the measuring point from the plume. As was discussed in the Section 3.4, in the Altiplano of northern Chile the studied volcanoes are located at high altitudes, with a very dry environment, very low relative humidity, and a thin atmosphere, which considerably reduces the dilution effect. We have estimated that for measurements carried out at distance <3 km the light dilution is negligible, as observed in the case of Olca volcano (Figure 3a), whereas for measurements <6 km light dilution seems to be somewhat important, producing underestimation lower than 20% (Table 2). Despite the limited effect of the light dilution on our measurements, this must be considered, especially in those measurements carried out at long distance, where the light dilution effects are more evident (Figure 3b; Table 2).

In order to compare OCV and CP image registration, we processed several sequences using both methods. Differences in plume speed mostly varied by 2% to 10.8%, although in exceptional cases they reached between 35.3% and 43.8%. In the case of SO_2 emission rates, a wider range of differences is found, from 0.6% to 28.2%, with a maximum difference of 50.3%. The low differences demonstrate that both methods are able to retrieve good quality data and broadly provide similar registration results. However, in the case of high differences, at times image alignment does not correctly register images with the OCV method, producing an overestimation of plume speed and SO_2 emission rates, as well as causing incorrect column amount retrievals due to incorrect off-band optical depth correction. The OCV method can produce errors in the alignment of the images, creating a false double plume, which is observed as a shadow of the original recorded plume and/or presence of artifacts, such as high SO_2 column density amounts in the volcanic edifice flanks or its borders (Figure 6a), similar to those observed previously with camera shake. This error is related to the occasional inability of the OCV method to automatically align the borders of the volcanic edifice; consequently, positive and negative differences could be produced by this error. Particularly, our data generates an overestimation of the SO_2 emission rates. The overestimation observed in our data can be avoided using the Control Points (CP) method, which allows manual alignment of the images from the two lenses, by use of control points in both images. These images produce a very well defined border of the volcanic edifice and, consequently, a very well defined gas plume (Figure 6b). Our data demonstrate that when image alignment cannot be reached using OCV post processing method, the use of CP method can produce a difference by at least 35% for SO_2 emission rates (Figure 7).

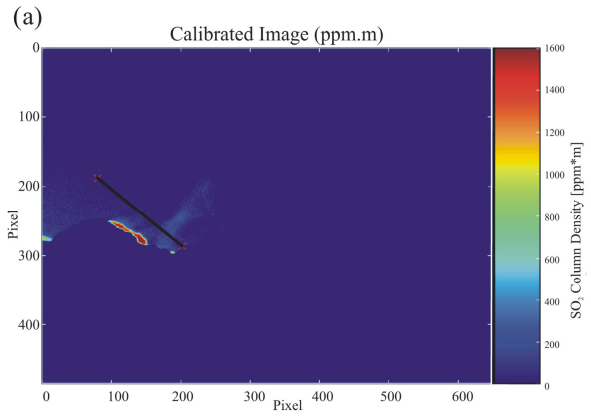

Figure 6. *Cont.*

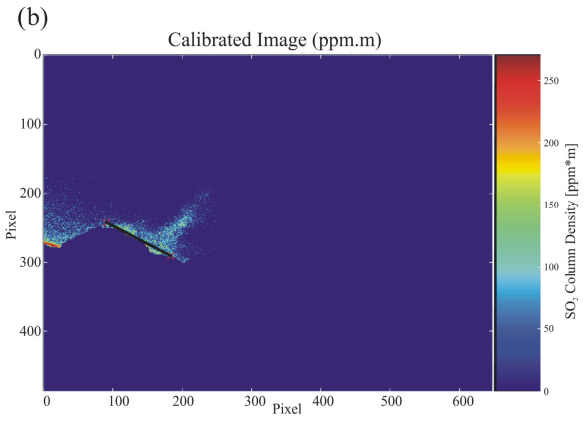

Figure 6. (**a**) Processed image from Irruputuncu volcano using OCV method showing a false high SO_2 column density amounts produced by a bad alignment of the camera A and B images; (**b**) Processed image from Irruputuncu volcano using CP method showing a good alignment of the camera A and B images (represented by the sharp borders of the volcanic edifice).

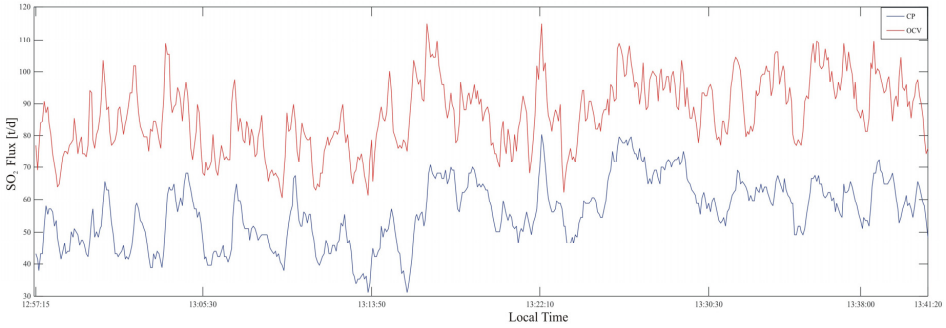

Figure 7. Data sequence 1 from Irruputuncu volcano (2 April 2018) showing the comparison between OCV and CP methods. Note that the OCV method produce an overestimation of the SO_2 emission rates due to the bad alignment of the images from the camera A and B, whereas a better SO_2 emission rate is obtained using CP method.

5.2. Comparison with Previous Measurements from Other Ground-Based Remote Techniques

Several authors have reported SO_2 emission rates from these studied volcanoes, mostly during discrete field campaigns with the DOAS techniques, but also with some prior use of UV cameras (Table 3). In contrast, Isluga volcano has been continuously monitored since December 2014 by OVDAS-SERNAGEOMIN using a permanent scanning DOAS station within the Network for Observation of Volcanic and Atmospheric Change (NOVAC) network (Table 3). In the case of Olca volcano, this is the first time that SO_2 rates have been reported using a ground-based remote sensing technique. In most cases, our SO_2 emission rates are lower than those reported by other authors, although in few cases our data are higher. A number of issues that could potentially impact upon acquired volcanic gas fluxes are listed below.

(1) Measurements of several plumes in a single volcano: in the case of Guallatiri volcano, which produces two plumes (from the southern flank and summit region respectively), Gliß et al. [1] reported SO_2 average outputs for the whole system of 112 ± 43.2 td^{-1}, and a maximum rate of 251 td^{-1}. In our case, we reported data exclusively for the summit region plume, with image sequence averages varying from 5.5 ± 2.8 to 50.5 ± 12.3 td^{-1}, and a maximum peak of 101 td^{-1}. However, these data are rather similar to those reported for just the summit plume by Gliß et al. [1], which ranged from 8.6 to 129 td^{-1} (Table 3), but in our case the span of fluxes is somewhat narrower. Indeed, differences in quoted emission rates can be attributed to the number of plumes considered at targets with multiple sources.

(2) Measuring points position, light dilution effect and plume geometry: the comparison between our data and those from other authors can also be related to camera orientation and distance from

the gas source. Indeed, this can influence the light dilution effect, which increases with this distance (e.g., [89,92]). Comparing data from Putana volcano reported by Tamburello et al. [40] and our measurements, differences could also be attributed to light dilution, as Tamburello et al. [40] measured 4.7 km from the summit fumaroles, whereas we worked up to 9.5 km from the source. Furthermore, it is ideal for UV camera measurements to be carried out viewing perpendicularly to the plume transport direction, due to the possibility that non-orthogonal measurements can produce notable differences in the SO_2 rates (e.g., [91]). Comparing data from Tamburello et al. [40] and Stebel et al. [41], and our measurements from Putana volcano during November 2017, the reported average SO_2 emission rates were 55.3 ± 17.3 td^{-1}, 40 ± 11 td^{-1}, and 31.9 ± 9.8 td^{-1}, respectively; in all cases measurements were carried out at a very similar distance to the same southernmost gas plume (between 4.7 and 6.2 km). Our data could therefore be underestimated since the plume motion was not perfectly perpendicular to our viewing orientation (~10 degrees), in contrast to Tamburello et al. [40] and Stebel et al. [41], who viewed almost perpendicularly to the plume transport vector. Additionally, our measurements were carried out during a cloudy day, which may have increased the humidity and, consequently, the light dilution effect. Considering that these differences are not very large, it is also possible to be attributed to natural volcanic variability.

Table 3. Data from other sources and techniques. 1 [1], 2 OVDAS-SERNAGEOMIN volcanic activity reports (www.sernageomin.cl), 3 [93], 4 [40], 5 [41]. (1) Peak in a single measurement sequence and/or daily peak, (2) calculated from monthly average reports, (3) overall after 3 days measurements, (4) optical flow post processing, (5) cross correlation post processing, n.r. not reported, * reported as a range.

Volcano	Date	Technique	SO_2 Emission Rate (td^{-1})		Reference
			Average	Maximum (1)	
Guallatiri (summit)	20–22 October 2014	UV Cam	8.6–129 *	129	1
Guallatiri (flank)	20–22 October 2014	UV Cam	n.r.	216	1
Guallatiri (whole system)	20–22 October 14	UV Cam	112 ± 43.2	251	1
Isluga (2)	2018	DOAS	199.2 ± 139.3	698	2
	2017	DOAS	270.7 ± 245.8	1841	2
	2016	DOAS	342.4 ± 323.3	1800	2
	2015	DOAS	339.9 ± 72.2	1600	2
	2014	DOAS	210	530	2
Irruputuncu	2004	DOAS	21–50 *	50	3
Ollagüe	2004	DOAS	4.5–9.1 *	9.1	3
	05/14	DOAS	150	n.r.	2
	11–2 December 2014	DOAS	150 ± 162	220 ± 181	4
San Pedro	10–12 December 2014	DOAS	161 ± 150	182 ± 188	4
	June 2014	DOAS	180	250	2
	May 2014	DOAS	190	n.r.	2
Putana	5, 6–12 December 2012	DOAS	97 ± 78 (3)	133 ± 104	4
	28 November 2012	UV Cam	60.5 ± 45.8 (4)	77.8 ± 51.8	5
	28 November 12	UV Cam	55.3 ± 17.3 (5)	121	5

(3) Seasonal effects: one of the most important factors that must be taken into account during discrete field campaigns are seasonal effects. Indeed, in our study area in northern Chile summer corresponds to the rainy and relatively hot season, influenced by Amazonian rains arriving from the east, and consequently producing relatively low-speed westward winds. On the contrary, autumn, winter, and spring correspond to dry and cold seasons, with faster eastward winds, with the fastest winds recorded during the end of autumn-early winter. A permanent NOVAC station (DOAS system) located on Isluga volcano and operative since December 2014, shows strong variations in the SO_2 emission rates, where differences can reach up to 656 td^{-1} in a single year and 685 td^{-1} for the whole period (Figure 8; Table 3); these variations are seen to oscillate on seasonal timescales. Explanations of these variations could be attributed to: (i) seasonal variations influencing the degassing pattern

of the studied volcanoes; (ii) inaccurate measurements from DOAS, possibly due to wind speed estimations or the location of the plume relative to the measuring instrument changing with the wind direction/speed; (iii) inaccurate measurements from both DOAS and UV cameras with some seasonal dependency. Since measurements between the UV camera and DOAS instruments are very similar when comparing data from the same season, we cautiously suggest that either point i or iii is valid here (Figure 8; Table 1; Table 3); however, long-term UV camera data is required to robustly test these hypotheses. Future investigations will be carried out in order to determine the extent of these seasonal effects in the volcanic degassing pattern in northern Chile volcanoes.

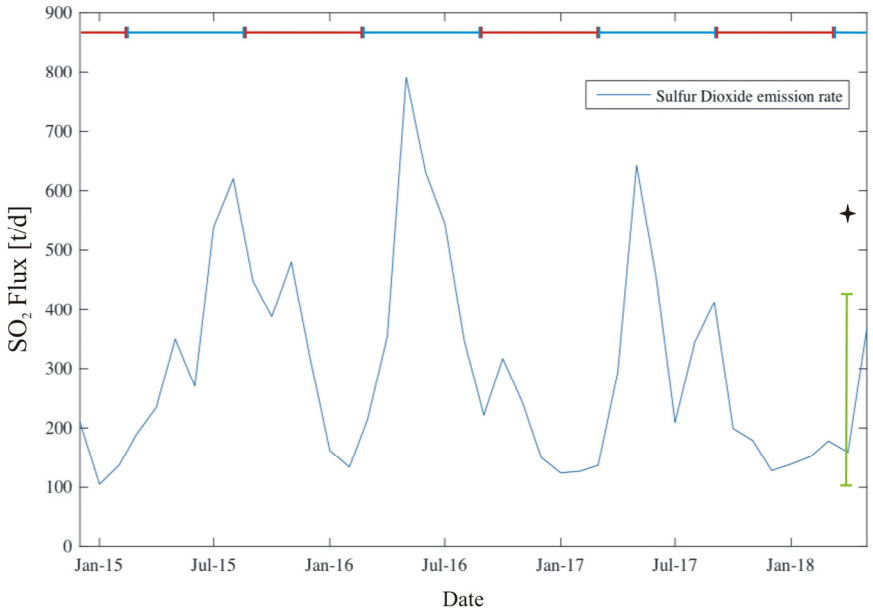

Figure 8. SO_2 emission rates of Isluga volcano from the permanent Network for Observation of Volcanic and Atmospheric Change (NOVAC) station showing monthly average from December 2014 to May 2018. Red bars show spring-summer seasons, blue bars show autumn-winter seasons, green bar shows SO_2 emission rates averages range from our measurements using the UV PiCam and the black star shows the maximum rate measured with the PiCam.

(4) Plume speed estimation and intrinsic errors of ground-based remote techniques: one of the most important sources of differences and errors in the calculation of SO_2 output corresponds to plume speed estimation. The UV camera has solved this problem by recording simultaneous images where plume movements can be tracked through time and consequently the plume speed can be accurately estimated. On the contrary, DOAS techniques need an external instrument and/or method to determine the plume speed. Atmospheric models, use of in-situ anemometers and even balloon sondes at airports are typically used to determine the plume speed (e.g., [5,40,94]), where more accurate information can be obtained if plume altitude is determined in the field during the measurements (considering layered atmospheric models depending of the altitude), which adds more uncertainties to the plume speed data. Additionally, the low density of meteorological stations in or close to the Altiplano has a consequence in global atmospheric models, which have poor resolution and hence lower accuracy in that area. Field wind speed determined on the ground, where measuring instruments are deployed, produce high uncertainties, since they are a coarse approximation to the atmospheric conditions where plume is transported away from the gas source, especially at high altitude volcanoes with high altitude differences between the volcano summit and its base and, consequently, strong differences exist in the wind speed at several altitudes. Ideally, a meteorological station deployed in the crater rim allows accurate estimations of plume speed and can be compared with UV camera estimations; nevertheless, there are no meteorological stations in any of the craters of the measured volcanoes in northern Chile. Data from DOAS on Isluga, Ollagüe, San Pedro, and Putana volcanoes differ widely with our data

(Table 3), and are characterized by its very high standard deviations, which could be partially attributed to the high variations in the plume speed estimations related with the method used to determine it, which are indirect and consequently inaccurate. In the case of Ollagüe, San Pedro, and Putana volcanoes, characterized by small and low intensity plumes, and a mix of several small plumes in the case of Putana volcano, SO_2 emission rates are particularly high. Here another factor can be added, corresponding to the differences in the "nature" of each technique, where several differences exist between the instruments characteristics. The UV camera is able to "see" the gas plume during the data acquisition, being capable of determining the plume speed simultaneously, and as we demonstrated previously, highly capable of detecting small plumes, even at long distances, as shown in the cases of Guallatiri and Putana, where plumes were measured at distances of 10.8 and 9.5 km, respectively (Table 1). On the contrary, the scanning pattern of DOAS technique is highly dependent on the plume geometry (as pointed in previously in Section 2), including its width, length, and propagation direction, and the size of the plume becomes highly important in long distance measurements. The addition of all these factors, including inaccurate plume speed determinations, can produce both under and overestimations of SO_2 emission rates, which could also add as a factor in the differences between our and previously reported data from northern Chile volcanoes.

5.3. Volcanological Implications of the SO_2 Emission Rates

SO_2 emission rates from the seven studied volcanoes can be preliminary divided into two groups: low and moderate emission rates volcanoes. Most of the studied volcanoes can be classified as displaying low emission rates, corresponding to the cases of Guallatiri, Olca, Ollagüe, San Pedro and Putana, with average rates being predominantly <20 td^{-1}. Those volcanoes emit fluids dominated by typical hydrothermal components, such as H_2S and CH_4, and relative low contents of SO_2 [33,95]. They are characterized by small gas plumes and the fumarolic emissions are related to lava domes or flows, where the gas is emitted from low temperature fumaroles (<84 °C). Only Guallatiri volcano has some high temperatures fumaroles (>200 °C), however, the fluid composition is dominated by hydrothermal components. Additionally, all these volcanoes have no records of historical eruptions, with the only exception of San Pedro volcano. The low SO_2 emission rates could be related to a long-lived passive degassing without eruptive activity over a very long period of time. On the contrary, moderate emission rate (>20 td^{-1}) volcanoes corresponds to Irruputuncu and Isluga volcano, with more abundance of magmatic components, like SO_2, high temperature fumaroles (>120 °C) and a larger gas plume [33]. Both volcanoes have records of eruptive activity in the last century, especially in the case of Isluga volcano, where its last crisis was recorded on 2003. In both cases, relatively moderate-to-high emission rates could be related to a higher level of activity, which could be correlated with more frequent eruptive activity in the records. Further studies must be carried out in order to confirm this classification, based on the combination of ground-based gas measurements and direct sampling of fumaroles. Additionally, the performance of frequent and prolonged surveys of ground-based techniques will help to improve the knowledge of the degassing pattern behavior of the studied volcanoes.

6. Conclusions

The PiCam UV camera has been successfully deployed on seven persistently degassing volcanoes from northern Chile, demonstrating the capacity to measure small and weak plumes (e.g., Olca and Putana volcanoes), as well as strongly degassing sources (e.g., Isluga volcano), resulting in resolution of SO_2 output rates ranging 3.8 ± 1.8–361 ± 31.6 td^{-1}, with measurements performed at a variety of distances from the gas sources (0.6–10.8 km). Given the low cost of the PiCam modules, with respect to traditionally applied scientific grade UV cameras, and the fact that these have delivered fail free service in these challenging field environments, over a protracted period of time, this affirms the suitability of these units for widespread dissemination to the end user community, worldwide. In addition, this article discusses additional factors relevant to all UV camera volcanic flux measurements: camera

shake, light dilution, and protocols adopted in post processing, in particular considering image registration used to calculate plume speeds and retrieve SO_2 rates. Differences in SO_2 emission rates by camera shake can be solved by removing the affected images and reprocessing the data, whereas although light dilution is observed in most of the measurements, its effects seems to be very limited, due to the thin, dry atmosphere at our high altitude study locations. For image registration, when the automated OCV algorithm is unable to correctly align the images from both cameras, the manual CP method can produce changes in the SO_2 rates of up to 35%. When a comparison is done between our data and reported remote ground-based techniques (such as DOAS, UV camera, and NOVAC permanent stations) in the volcanoes presented here (except Olca), differences (in most cases our emission rates are lower) can be attributed to (i) measuring of single plumes in multi-plume volcanoes, (ii) instrument-plume distance and consequently the light dilution effect, (iii) the geometry of the plume measured, (iv) seasonal effects, and (v) the methods used to calculate the plume speed. In most of the cases, we suggest that the larger SO_2 emission rates from reported data are related to methods used to calculate the plume speed and strong seasonal effects. Finally, we define two distinct groups of volcanoes according to the SO_2 emission rates: low and moderate, which correlate positively with volcanological characteristics. Volcanoes defined as having low SO_2 emission rates (<20 t d^{-1}) are systems dominated by hydrothermal fluids; magmatic dominated fluids systems produce moderate SO_2 rate plumes (>20 t d^{-1}).

Supplementary Materials: The following are available online at http://www.mdpi.com/2072-4292/12/13/2122/s1, Figure S1: Mosaic of Landsat OLI satellite images in combination 742 (RGB) showing the measuring points (yellow filled circles), active craters-fumarolic fields (red filled triangles) and direction of plume measured (red dashed arrows) for (a) Guallatiri, (b) Isluga, (c) Irruputuncu, (d) Olca, (e) Ollagüe, (f) San Pedro and (g) Putana volcanoes, Figure S2: Mosaic of an example of processed image (column 1) and field photography (column 2) of the volcanoes measured for this work, corresponding to (a) Guallatiri, (b) Isluga, (c) Irruputuncu, (d) Olca, (e) Ollagüe, (f) San Pedro and (g) Putana volcanoes, Video S3: Stop motion of a whole sequence of San Pedro volcano showing the effects of the camera shake.

Author Contributions: F.A., S.L., and T.C.W. wrote the paper. F.A., S.L., F.R., P.A., C.G., M.I., and G.U. performed field measurements. F.R., P.A., C.G., and M.I. processed data. T.C.W., T.D.P., and A.J.S.M. built the U.V. camera, wrote the code, and reviewed the manuscript. All authors have read and agreed to the published version of the manuscript.

Funding: This research was partially funded by VRIDT-UCN Proyectos Especiales 2017 "Procesos que controlan el balance de masa en volcanes activos del norte de Chile" (FA, FR, and PA) and CONICYT-PCHA/Doctorado Nacional/2016-21160276 (SL). CG, MI, and GU are funded by CONICYT-PCHA/Doctorado Nacional/2016-21160176, 2016-21160172, and 2016-21161286 projects, respectively.

Acknowledgments: Our acknowledgments to Álvaro Vergara (Núcleo de Investigación en Riesgo Volcánico-Ckelar Volcanes) and José Sepúlveda (University of Florence, Italy) by their support in the fieldwork.

Conflicts of Interest: The authors declare no conflict of interest.

References

1. Gliß, J.; Stebel, K.; Kylling, A.; Sudbo, A. Improved optical flow velocity analysis in SO_2 camera images of volcanic plumes—Implications for emission-rate retrievals investigated at Mt Etna, Italy and Guallatiri, Chile. *Atmos. Meas. Tech.* **2018**, *11*, 781–801. [CrossRef]
2. Giggenbach, W. Chemical composition of volcanic gases. In *Monitoring and mitigation of Volcano Hazards*; Scarpa, R., Tilling, R., Eds.; Springer-Verlag: Berlin, Germany, 1996; pp. 222–256.
3. Symonds, R.B.; Rose, W.I.; Bluth, G.J.S.; Gerlach, T.M. Volcanic gas studies: Methods, results and applications. In *Volatiles in Magmas*; Carroll, M.R., Hollaway, J.R., Eds.; Mineralogical Society of America: Washington, DC, USA, 1994; pp. 1–66.
4. Smekens, J.F.; Burton, M.R.; Clarke, A. Validation of the SO_2 camera for high temporal and spatial resolution monitoring of SO_2 emissions. *J. Volcanol. Geotherm. Res.* **2015**, *300*, 37–47. [CrossRef]
5. Rodríguez, L.; Nadeau, P. Resumen de las principales técnicas de percepción remota usadas en volcanes para monitorear las emisiones de gas en la superficie. *Rev. Geol. Am. Central.* **2015**, *52*, 67–105.

6. Krotkov, N.A.; Torres, O.; Seftor, C.; Krueger, A.J.; Rose, W.; Kostinski, A.; Bluth, G.; Schneider, D.; Schaefer, S.J. Comparison of TOMS and AVHRR volcanic ash retrievals from the August 1992 eruption of Mt. Spurr. *Geophys. Res. Lett.* **1999**, *26*, 455–458. [CrossRef]
7. Carn, S.A.; Krueger, A.J.; Bluth, G.S.J.; Schaefer, S.J.; Krotkov, N.A.; Watson, I.M.; Datta, S. Volcanic eruption detection by the Total Ozone Mapping Spectrometer (TOMS) instruments: A 22-year record of sulphur dioxide and ash emissions. In *Volcanic Degassing*; Oppenheimer, C., Pyle, D.M., Barclay, J., Eds.; Geological Society: London, UK, 2003; pp. 177–202.
8. Carn, S.; Kroktov, N.; Yang, K.; Krueger, A. Measuring global volcanic degassing with the Ozone Monitoring Instrument (OMI). In *Remote Sensing of Volcanoes and Volcanic Processes: Integrating Observation and Modelling*; Mather, T., Biggs, J., Eds.; Geological Society: London, UK, 2013; Volume 380.
9. Carn, S.; Fioletov, V.; McLinden, C.; Li, C.; Krotov, N. A decade of global volcanic SO_2 emissions measured from space. *Sci. Rep. Sci. Rep.* **2017**, *7*, 44095. [CrossRef] [PubMed]
10. Moussallam, Y.; Peters, N.; Masias, P.; Apaza, F.; Barnie, T.; Schipper, C.I.; Curtis, A.; Tamburello, G.; Aiuppa, A.; Bani, P.; et al. Magmatic gas percolation through the old lava dome of El Misti volcano. *Bull. Volcanol.* **2017**, *79*, 46. [CrossRef] [PubMed]
11. Vaselli, O.; Tassi, F.; Montegrossi, G.; Capaccioni, B.; Giannini, L. Sampling and analysis of fumarolic gases. *Acta Vulcanol.* **2006**, *18*, 65–76.
12. Caltabiano, T.; Romano, R.; Budetta, G. SO_2 measurements at Mount Etna, Sicily. *J. Volcanol. Geotherm. Res.* **1994**, *99*, 12.809–12.811.
13. Galle, B.; Oppenheimer, C.; Geyer, A.; McGonigle, A.J.S.; Edmonds, M.; Horrocks, L.A. A miniaturised UV spectrometer for remote sensing of SO_2 fluxes: A new tool for volcano surveillance. *J. Volcanol. Geotherm. Res.* **2003**, *119*, 241–254. [CrossRef]
14. McGonigle, A.J.S.; Oppenheimer, C.; Galle, B.; Mather, T.A.; Pyle, D.M. Walking traverse and scanning DOAS measurements of volcanic gas emission rates. *Geophys. Res. Lett.* **2002**, *29*, 1985. [CrossRef]
15. Oppenheimer, C.; Bani, P.; Calkins, J.A.; Burton, M.R.; Sawyer, G.M. Rapid FTIR sensing of volcanic gases released by strombolian explosions at Yasur volcano, Vanuatu. *Appl. Phys. B* **2006**, *85*, 453–460. [CrossRef]
16. Mori, T.; Notsu, K. Temporal variation in Chemicals composition of the volcanic plume from Aso volcano, Japan, measured by remote FTIR spectroscopy. *Geochem. J.* **2008**, *42*, 133–140. [CrossRef]
17. Prata, A.J.; Bernardo, C. Retrieval of sulphur dioxide from a ground-based thermal infrared Imaging camera. *Atmos. Meas. Tech.* **2014**, *7*, 1153–1211. [CrossRef]
18. Kern, C.; Lubcke, P.; Bobrowski, N.; Campion, R.; Mori, T.; Smekens, J.F.; Stebel, K.; Tamburello, G.; Burton, M.R.; Platt, U.; et al. Intercomparison of SO_2 camera systems for imaging volcanic gas plumes. *J. Volcanol. Geotherm. Res.* **2015**, *300*, 22–36. [CrossRef]
19. Calabrese, S.; Aiuppa, S.; Allard, P.; Bagnato, E.; Bellomo, S.; Brusca, L.; D'Alessandro, W.; Parello, F. Atmospheric sources and sinks of volcanogenic elements in a basaltic volcano (Etna, Italy). *Geochim. Cosmochim. Acta* **2011**, *75*, 7401–7425. [CrossRef]
20. Mather, T.A.; Witt, M.L.I.; Pyle, D.M.; Quayle, B.M.; Aiuppa, A.; Bagnato, E.; Martin, R.S.; Sims, K.W.W.; Edmonds, M.; Sutton, A.J.; et al. Halogens and trace metal emissions from the ongoing 2008 summit eruption of Kīlauea volcano, Hawai'i. *Geochim. Cosmochim. Acta* **2012**, *83*, 292–323. [CrossRef]
21. McElhoe, H.B.; Conner, W.D. Remote Measurement of Sulfur dioxide emissions using an Ultraviolet Light sensitive video system. *J. Air Pollut. Control Assoc.* **1986**, *36*, 42–47. [CrossRef]
22. Mori, T.; Burton, M.R. The SO_2 camera: A simple, fast and cheap method for ground-based imaging of SO_2 in volcanic plumes. *Geophys. Res. Lett.* **2006**, *33*, L24804. [CrossRef]
23. Bluth, G.; Shannon, J.; Watson, I.M.; Prata, A.J.; Realmuto, V. Development of an ultra-violet digital camera for volcanic SO_2 imaging. *J. Volcanol. Geotherm. Res.* **2007**, *161*, 47–56. [CrossRef]
24. Moussallam, Y.; Bani, P.; Curtis, A.; Barnie, T.; Moussallam, M.; Peters, N.; Schipper, C.I.; Aiuppa, A.; Giudice, G.; Amigo, Á.; et al. Sustaining persistent lava lakes: Observations from high-resolution gas measurements at Villarrica volcano, Chile. *Earth Planet. Sci. Lett.* **2016**, *454*, 237–247. [CrossRef]
25. Pering, T.D.; McGonigle, A.J.S.; James, M.R.; Tamburello, G.; Aiuppa, A.; Delle Donne, D.; Ripepe, M. Conduit dynamics and post explosion degassing on Stromboli: A combined UV camera and numerical modelling treatment. *Geophys. Res. Lett.* **2016**, *43*, 5009–5016. [CrossRef] [PubMed]

26. Delle Donne, D.; Ripepe, M.; Lacanna, G.; Tamburello, G.; Bitetto, M.; Aiuppa, A. Gas mass derived by infrasound and UV cameras: Implications for mass flow rate. *J. Volcanol. Geotherm. Res.* **2016**, *325*, 169–178. [CrossRef]
27. Kazahaya, R.; Mori, T.; Takeo, M.; Ohminato, T.; Urabe, T.; Maeda, Y. Relation between single very-long-period pulses and volcanic gas emissions at Mt. Asama, Japan. *Geophys. Res. Lett.* **2011**, *38*, L11307. [CrossRef]
28. Nadeau, P.A.; Palma, J.L.; Waite, G.P. Linking volcanic tremor, degassing, and eruption dynamics with SO_2 imaging. *Geophys. Res. Lett.* **2011**, *38*, L013404. [CrossRef]
29. Burton, M.R.; Salerno, G.G.; D'Auria, L.; Caltabiano, T.; Murè, F.; Maugeri, R. SO_2 flux monitoring at Stromboli with the new permanent INGV SO_2 camera system: A comparison with the FLAME network and seismological data. *J. Volcanol. Geotherm. Res.* **2015**, *300*, 95–102. [CrossRef]
30. Wilkes, T.C.; McGonigle, A.J.S.; Pering, T.D.; Taggart, A.J.; White, B.S.; Bryant, R.G.; Willmott, J.R. Ultraviolet imaging with low cost smartphone sensors: Development and application of a raspberry Pi-based UV camera. *Sensors* **2016**, *16*, 1649. [CrossRef] [PubMed]
31. Wilkes, T.C.; Pering, T.D.; McGonigle, A.J.S.; Tamburello, G.; Willmott, J.R. A low-cost smartphone sensor-based UV camera for volcanic SO_2 emission measurements. *Remote Sens.* **2017**, *9*, 27. [CrossRef]
32. Tassi, F.; Aguilera, F.; Vaselli, O.; Medina, E.; Tedesco, D.; Huertas, A.D.; Poreda, R.; Kojima, S. The magmatic-and hydrothermal-dominated fumarolic system at the active crater of Lascar volcano, northern Chile. *Bull. Volcanol.* **2009**, *71*, 171–183. [CrossRef]
33. Tassi, F.; Aguilera, F.; Vaselli, O.; Darrah, T.; Medina, E. Gas discharges from four remote volcanoes in northern Chile (Putana, Olca, Irruputuncu and Alitar): A geochemical survey. *Ann. Geophys. Italy* **2011**, *54*, 121–136.
34. Capaccioni, B.; Aguilera, F.; Tassi, F.; Darrah, T.; Poreda, R.; Vaselli, O. Geochemical and isotopic evidences of magmatic inputs in the hydrothermal reservoir feeding the fumarolic discharges of Tacora volcano (northern Chile). *J. Geotherm. Res.* **2011**, *208*, 77–85. [CrossRef]
35. Aguilera, F.; Tassi, F.; Darrah, T.; Moune, S.; Vaselli, O. Geochemical model of a magmatic hydrothermal system at the Lastarria volcano, northern Chile. *Bull. Volcanol.* **2012**, *74*, 119–134. [CrossRef]
36. Menard, G.; Moune, S.; Vlastélic, I.; Aguilera, F.; Valade, S.; Bontemps, M.; González, R. Gas and aerosol emissions from Lascar volcano (Northern Chile): Insights into the origen of gases and their links with the volcanic activity. *J. Volcanol. Geotherm. Res.* **2014**, *287*, 51–67. [CrossRef]
37. Andres, R.; Rose, W.; Kyle, P.; de Silva, S.; Francis, P.; Gardeweg, M.; Moreno, H. Excessive sulfur dioxide emissions from Chilean volcanoes. *J. Volcanol. Geotherm. Res.* **1991**, *46*, 323–329. [CrossRef]
38. Mather, T.; Tsanev, V.I.; Pyle, D.M.; McGonigle, A.J.S.; Oppenheimer, C.; Allen, A.G. Characterization and evolution of tropospheric plumes from Lascar and Villarrica volcanoes, Chile. *J. Geophys. Res.* **2004**, *109*, D21303. [CrossRef]
39. Geoffroy, C. Estimación de la emisión de dióxido de azufre en penachos volcánicos mediante una cámara ultravioleta. Undergraduate Thesis, Universidad de Chile, Santiago, Chile, 2014. Available online: http://repositorio.uchile.cl/bitstream/handle/2250/117055/cf-geoffroy_cg.pdf?sequence=1&isAllowed=y (accessed on 30 June 2020).
40. Tamburello, G.; Hansteen, T.H.; Bredemeyer, S.; Aiuppa, A.; Tassi, F. Gas emissions from five volcanoes in northern Chile and implications for the volatiles budget of the Central Volcanic Zone. *Geophys. Res. Lett.* **2014**, *41*, 4961–4969. [CrossRef]
41. Stebel, K.; Amigo, A.; Thomas, H.E.; Prata, A.J. First estimates of fumarolic SO_2 fluxes from Putana volcano, Chile, using an ultraviolet imaging camera. *J. Volcanol. Geotherm. Res.* **2015**, *300*, 112–120. [CrossRef]
42. Lopez, T.; Aguilera, F.; Tassi, F.; de Moore, M.J.; Bobrowski, N.; Aiuppa, A.; Tamburello, G.; Rizzo, A.; Liuzzo, M.; Viveiros, F.; et al. New constraints on the magmatic-hydrothermal system and volatile budget of Lastarria Volcano, Chile: Integrated results from the 2014 IAVCEI CCVG 12th Volcanic Gas Workshop. *Geosphere* **2018**, *14*, 983–1007. [CrossRef]
43. DeMets, C.; Gordon, R.G.; Argus, D.F.; Stein, S. Current plate motions. *Geophys. J. Int.* **1990**, *101*, 425–478. [CrossRef]
44. Stern, C.; Moreno, H.; López-Escobar, L.; Clavero, J.; Lara, L.; Naranjo, J.; Parada, M.; Skewes, M. Chilean volcanoes. In *The Geology of Chile*; Moreno, T., Gibbons, W., Eds.; The Geological Society: London, UK, 2007; pp. 147–178.

45. Syracuse, E.M.; Abers, G.A. Global compilation of variations in slab depth beneath arc volcanoes and implications. *Geochem. Geophys. Geosyst.* **2006**, *7*, 1–18. [CrossRef]
46. Stern, C.R. Active Andean volcanism: Its geologic and tectonic setting. *Rev. Geol. Chile* **2004**, *31*, 161–206. [CrossRef]
47. de Silva, S.L.; Francis, P.W. *Volcanoes of the central Andes*; Springer-Verlag: Heidelberg, Germany, 1991; p. 216.
48. González-Ferran, O. *Volcanes de Chile*; Instituto Geográfico Militar: Santiago, Chile, 1995; p. 639.
49. Siebert, L.; Simkin, T.; Kimberly, P. *Volcanoes of the World*, 3rd ed.; University of California Press: Berkeley, CA, USA, 2010; p. 551.
50. Lucassen, F.; Becchio, R.; Kasemann, S.; Franz, G.; Trumbull, R.; Wilke, H.; Romer, R.; Dulski, F. Composition and density model of the continental crust at an active continental margin- the Central Andes between 21° and 27°S. *Tectonophysics* **2001**, *341*, 195–223. [CrossRef]
51. Wörner, G.; Hammerschmidt, K.; Henjes-Kunst, F.; Lezaun, J.; Wilke, H. Geochronology (40Ar/39Ar, K-Ar and He-exposure ages) of Cenozoic magmatic rocks from northern Chile (18–22 S): Implications for magmatism and tectonic evolution of the central Andes. *Rev. Geol. Chile* **2000**, *27*, 205–240.
52. Allmendinger, R.; Jordan, T.; Kay, S.; Isacks, B. The evolution of the Altiplano-Puna Plateau of The Central Andes. *Annu. Rev. Earth Planet. Sci.* **1997**, *25*, 139–174. [CrossRef]
53. Yuan, X.; Sobolev, S.V.; Kind, R. Moho topography in the central Andes and its geodynamic implications. *Earth Planet. Sci. Lett.* **2002**, *199*, 389–402. [CrossRef]
54. Wörner, G.; Lopez-Escobar, L.; Moorbath, S.; Horn, S.; Entenmann, J.; Harmon, R.; Davidson, J. Variaciones geoquímicas, locales y regionales, en el frente volcánico cuaternario de los Andes Centrales (17 30'–22 00'S), Norte de Chile. *Andean Geol.* **1992**, *19*, 37–56.
55. Wörner, G.; Moorbath, S.; Horn, S.; Entenmann, J.; Harmon, R.; Davidson, J.; Lopez-Escobar, L. Large-and fine-scale geochemical variations along the Andean arc of northern Chile (17.5–22 S). In *Tectonics of the southern Central Andes*; Reutter, K.J., Scheuber, E., Wigger, P., Eds.; Springer: Berlin/Heidelberg, Germany, 1994; pp. 77–92.
56. Aitcheson, S.; Harmon, R.; Moorbath, S.; Schneider, A.; Soler, P.; Soria-Escalante, E.; Steele, G.; Awainbank, I.; Wörner, G. Pb isotopes define basement domains of the Altiplano, central Andes. *Geology* **1995**, *23*, 555–558. [CrossRef]
57. Mamani, M.; Tassara, A.; Wörner, G. Composition and structural control of crustal domains in the central Andes. *Geochem. Geophy. Geosyst.* **2008**, *9*, 1–13. [CrossRef]
58. Mamani, M.; Wörner, G.; Sempere, T. Geochemical variations in igneous rocks of the Central Andean orocline (13°S to 18°S): Tracing crustal thickening and magma generation through time and space. *Geol. Soc. Am. Bull.* **2010**, *122*, 162–182. [CrossRef]
59. Lucassen, F.; Becchio, R.; Franz, G. The Early Palaeozoic high-grade metamorphism at the active continental margin of West Gondwana in the Andes (NW Argentina/N Chile). *Int. J. Earth Sci.* **2011**, *100*, 445–463. [CrossRef]
60. Casertano, L. General characteristics of active Andean volcanoes and a summary of their activities during recent centuries. *Bull. Seismol Soc. Am.* **1963**, *53*, 1415–1433.
61. Tassi, F.; Aguilera, F.; Darrah, F.; Vaselli, O.; Capaccioni, B.; Poreda, R.J.; Delgado Huertas, A. Fluid geochemistry of hydrothermal systems in the Arica-Parinacota, Tarapacá and Antofagasta regions (northern Chile). *J. Volcanol. Geotherm. Res.* **2010**, *192*, 1–15. [CrossRef]
62. Global Volcanism Program. In Global Volcanism Program, Irruputuncu (Chile-Bolivia): Minor, Late-1995 Eruption; the First Unambiguous Modern Report. 1997. Available online: https://volcano.si.edu/showreport.cfm?doi=10.5479/si.GVP.BGVN199701-355040 (accessed on 30 June 2020).
63. Céspedes, L.; Clavero, J.; Cayupi, J. Hazard management at Isluga volcano, northern Chile: Preliminary results. In Proceedings of the IAVCEI General Assembly, Pucón, Chile, 14–16 November 2004.
64. Global Volcanism Program. In Global Volcanism Program, Lascar (Chile): Eruptions Sends Ash above 25 km Altitude; Pyroclastic Flow Travel 7.5 km. Available online: https://volcano.si.edu/showreport.cfm?doi=10.5479/si.GVP.BGVN199304-355100 (accessed on 30 June 2020).
65. Gardeweg, M.C.; Medina, E. La erupción subpliniana del 19-20 de Abril de 1993 del Volcán Lascar, N. de Chile. In Proceedings of the 7th Chilean Geological Congress, Concepción, Chile, 17–21 October 1994.

66. Global Volcanism Program. In Global Volcanism Program, Lascar (Chile): Small Ash Eruptions and Increased Height of Gas Plume. Available online: https://volcano.si.edu/showreport.cfm?doi=10.5479/si.GVP.BGVN199503-355100 (accessed on 30 June 2020).
67. Global Volcanism Program. In Global Volcanism Program, Lascar (Chile): Ash Eruption on 20–21 July. Available online: https://volcano.si.edu/showreport.cfm?doi=10.5479/si.GVP.BGVN200006-355100 (accessed on 30 June 2020).
68. Global Volcanism Program. In Global Volcanism Program, Lascar (Chile): Further Analysis of 4 May 2005 Event Indicates A Phreato-Vulcanian Eruption. Available online: https://volcano.si.edu/showreport.cfm?doi=10.5479/si.GVP.BGVN200505-355100 (accessed on 30 June 2020).
69. Global Volcanism Program. In Global Volcanism Program, Lascar (Chile): Seismicity, Glow, Gray Plumes, and Other Anomalies Suggest April 2013 Eruption. Available online: https://volcano.si.edu/showreport.cfm?doi=10.5479/si.GVP.BGVN201307-355100 (accessed on 30 June 2020).
70. Global Volcanism Program. In Global Volcanism Program, Lascar (Chile): Ash Plume on 30 October 2015 Rises 2500 m high; Variable Seismicity and Persistent Thermal Anomaly afterwards. Available online: https://volcano.si.edu/showreport.cfm?doi=10.5479/si.GVP.BGVN201607-355100 (accessed on 30 June 2020).
71. Sepúlveda, J.; Inostroza, M.; Esquivel, A. Evolución Geológica del Complejo Volcánico Guallatiri, región de Arica y Parinacota, norte de Chile. In Proceedings of the XV Congreso Geológico Chileno, Concepción, Chile, 18–23 November 2018.
72. Inostroza, M.; Aguilera, F.; Tassi, F.; Cappecciachi, F.; Sepúlveda, J.; González, C.; Ureta, G.; Layana, S. Preliminary assessment of the origin and evolution of fluids discharged from Guallatiri volcano, Cities on Volcanoes 10, Naples, Italy, 2–7 September 2018.
73. Cortés, J.; Cascante, M.; Zavala, V. *Geología de las Áreas Isluga y Sierra de Huaillas, Región de Tarapacá*; Serie Geología Básica; Servicio Nacional de Geología y Minería: Santiago, Chile, 2014; pp. 172–173.
74. Cascante, M. Evolución Geológica y Magmática del Volcán Isluga 19°S. Región de Tarapacá, Chile. Master's Thesis, Universidad de Chile, Santiago, Chile, 2015.
75. Rodríguez, I.; Roche, O.; Moune, S.; Aguilera, F.; Campos, E.; Pizarro, M. Evolution of Irruputuncu volcano, central Andes, northern Chile. *J. S. Am. Earth Sci.* **2015**, *63*, 385–399. [CrossRef]
76. Aguilera, F. *Origen Y Naturaleza De Los Fluidos En Los Sistemas Volcánicos, Geotermales Y Termales De Baja Entalpía De La Zona Volcánica Central (zvc) Entre Los 17°43′S Y 25°10′S*; Fundación Bicentenario: Santiago, Chile, 2010; p. 307.
77. Gardeweg, M.; Selles, D.; Arcos, R.; Pino, H.; Camacho, J.; Sprohnle, C.; Sanhueza, A.; Mont, A. Volcanismo del Cenozoico tardío al este de Collahuasi, Región de Tarapacá, Chile. In Proceedings of the XII Congreso Geológico Chileno, Santiago, Chile, 22–26 November 2009.
78. Martínez, S.; Navas, S.; González, C.; Aguilera, F. *Geología del Complejo Volcánico Olca-Paruma, Norte de Chile, Actas 12º Encuentro del Centro Internacional de Ciencias de la Tierra, Mendoza, Argentina, November 2017*; Gomez, M.P., Lopez, M.I., Eds.; International Center for Earth Sciences: Buenos Aires, Argentina, 2018.
79. Godoy, B.; Wörner, G.; Kojima, S.; Aguilera, F.; Simon, K.; Hartmann, G. Low-pressure evolution of arc magmas in thickened crust: The San Pedro-Linzor volcanic chain, Central Andes, Northern Chile. *J. S. Am. Earth Sci.* **2014**, *52*, 24–42. [CrossRef]
80. Francis, P.; Roobol, M.; Walker, G.; Cobbold, P.; Coward, M. The San Pedro and San Pablo volcanoes of northern Chile and their hot avalanche deposits. *Geol. Rundsch.* **1974**, *63*, 357–388. [CrossRef]
81. O'Callaghan, L.; Francis, P. Volcanological and petrological evolution of San Pedro volcano, Provincia El Loa, North Chile. *J. Geol. Soc. Lond.* **1986**, *143*, 275–286. [CrossRef]
82. Amigo, A.; Bertin, D.; Orozco, G. *Peligros Volcánicos de la Zona Norte de Chile, Regiones de Arica y Parinacota, Tarapacá, Antofagasta y Atacama*; Serie 177; Servicio Nacional de Geología y Minería: Santiago, Chile, 2012; p. 45.
83. Bruggen, J. *Fundamentos de la Geología en Chile*; Instituto Geográfico Militar: Santiago, Chile, 1950; p. 374.
84. Petit-Breuilh, M.E. *La historia eruptiva de los volcanes hispanoamericanos (Siglos XVI al XX)*; Casa de los volcanes: Huelva, Spain, 2004; p. 431.
85. Martin, C. Los volcanes activos de Chile. *Rev. Chil. Hist. Nat.* **1901**, *5*, 243–250.
86. Marinovic, N.; Lahsen, A. *Hoja Calama: Región de Antofagasta*; Serie 58; Servicio Nacional de Geología y Minería: Santiago, Chile, 1984; p. 140.
87. Kantzas, E.P.; McGonigle, A.J.; Tamburello, G.; Aiuppa, A.; Bryant, R.G. Protocols for UV camera volcanic SO_2 measurements. *J. Volcanol. Geotherm. Res.* **2010**, *194*, 55–60. [CrossRef]

88. Gliß, J.; Stebel, K.; Kylling, A.; Dinger, A.; Sihler, H.; Sudbø, A. A Python Software Toolbox for the Analysis of SO_2 Camera Data. Implications in geosciences. *Geosciences* **2017**, *7*, 134. [CrossRef]
89. Campion, R.A.; Delgado-Granados, H.; Mori, T. Image-based correction of the light dilution effect for SO_2 camera measurements. *J. Volcanol. Geotherm. Res.* **2015**, *300*, 48–57. [CrossRef]
90. Llanko, T.; Pering, T.; Wilkes, T.; Apaza Choquehuayta, F.; Kern, C.; Diaz Moreno, A.; De Angelis, S.; Layana, S.; Rojas, F.; Aguilera, F.; et al. Degassing at Sabancaya volcano measured by UV cameras and the Novak network. *Volcanica* **2019**, *2*, 239–252.
91. Klein, A.; Lübcke, P.; Bobrowski, N.; Kuhn, J.; Platt, U. Plume propagation direction determination with SO_2 cameras. *Atmos. Meas. Tech.* **2017**, *10*, 979–987. [CrossRef]
92. Kern, C.; Kick, F.; Lübcke, P.; Vogel, L.; Wöhrbach, M.; Platt, U. Theoretical description of Functionality, Applications, and Limitations of SO_2 Cameras for the Remote Sensing of volcanic Plumes. *Atmos. Meas. Tech.* **2010**, *3*, 733–749. [CrossRef]
93. Clavero, J.; Soler, V.; Amigo, A. Caracterizacion preliminar de la actividad sismica y de desgasificacion pasiva de volcanes activos de los Andes Centrales del norte de Chile. In Proceedings of the Actas 11º Congreso Geologico Chileno, Antofagasta, Chile, 7–11 August 2006.
94. Johansson, M.; Galle, B.; Zhang, Y.; Rivera, C.; Chen, D.; Wyser, K. The dual-beam mini-DOAS technique–measurements of volcanic gas emission, plume height and plume Speedy with a single instrument. *Bull. Volcanol.* **2009**, *71*, 747–751. [CrossRef]
95. Inostroza, M.; Tassi, F.; Aguilera, F.; Sepúlveda, J.; Capecchiacci, F.; Venturi, S.; Capasso, G. Geochemistry of gas and water discharges from the magmatic-hydrothermal system of the Guallatiri Volcano, northern Chile. *Bull. Volcanol.* **2020**, in press. [CrossRef]